



Delft University of Technology

A multi-year cross-validation experiment for estimating rice plant area index (PAI) over the JECAM-India test site from simulated RADARSAT constellation mission (RCM) compact polarimetric SAR data

Mandal, Dipankar; Kumar, Vineet; Bhattacharya, Avik; McNairn, Heather; Rao, Yalamanchili S.

DOI

[10.1080/01431161.2021.1999528](https://doi.org/10.1080/01431161.2021.1999528)

Publication date

2021

Document Version

Final published version

Published in

International Journal of Remote Sensing

Citation (APA)

Mandal, D., Kumar, V., Bhattacharya, A., McNairn, H., & Rao, Y. S. (2021). A multi-year cross-validation experiment for estimating rice plant area index (PAI) over the JECAM-India test site from simulated RADARSAT constellation mission (RCM) compact polarimetric SAR data. *International Journal of Remote Sensing*, 42(24), 9515-9547. <https://doi.org/10.1080/01431161.2021.1999528>

Important note

To cite this publication, please use the final published version (if applicable).

Please check the document version above.

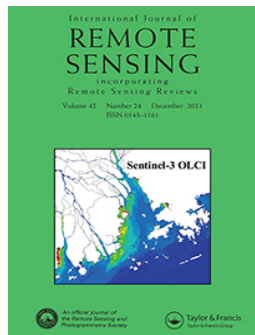
Copyright

Other than for strictly personal use, it is not permitted to download, forward or distribute the text or part of it, without the consent of the author(s) and/or copyright holder(s), unless the work is under an open content license such as Creative Commons.

Takedown policy

Please contact us and provide details if you believe this document breaches copyrights.

We will remove access to the work immediately and investigate your claim.



A multi-year cross-validation experiment for estimating rice plant area index (PAI) over the JECAM-India test site from simulated RADARSAT constellation mission (RCM) compact polarimetric SAR data

Dipankar Mandal, Vineet Kumar, Avik Bhattacharya, Heather McNairn & Yalamanchili S. Rao

To cite this article: Dipankar Mandal, Vineet Kumar, Avik Bhattacharya, Heather McNairn & Yalamanchili S. Rao (2021) A multi-year cross-validation experiment for estimating rice plant area index (PAI) over the JECAM-India test site from simulated RADARSAT constellation mission (RCM) compact polarimetric SAR data, International Journal of Remote Sensing, 42:24, 9490-9522, DOI: [10.1080/01431161.2021.1999528](https://doi.org/10.1080/01431161.2021.1999528)

To link to this article: <https://doi.org/10.1080/01431161.2021.1999528>



Published online: 22 Nov 2021.



Submit your article to this journal



Article views: 70



View related articles



View Crossmark data



A multi-year cross-validation experiment for estimating rice plant area index (PAI) over the JECAM-India test site from simulated RADARSAT constellation mission (RCM) compact polarimetric SAR data

Dipankar Mandal ^{a,b}, Vineet Kumar ^c, Avik Bhattacharya ^a, Heather McNairn ^d and Yalamanchili S. Rao^a

^aMicrowave Remote Sensing Lab, Centre of Studies in Resources Engineering, Indian Institute of Technology Bombay, Mumbai, India; ^bDepartment of Agronomy, Kansas State University, Manhattan, Kansas, USA;

^cDepartment of Water Resources, Delft University of Technology, Delft, The Netherlands; ^dOttawa Research and Development Centre, Agriculture and Agri-Food Canada, Ottawa, Canada

ABSTRACT

Using the cross-validation approach, strategies for estimating biophysical parameters are still pre-operational with synthetic aperture radar (SAR) data. In this regard, the Joint Experiment for Crop Assessment and Monitoring (JECAM) SAR inter-comparison experiments provide an opportunity for the potential implementation of cross-validation strategies for biophysical parameters retrieval utilizing the next-generation compact polarimetric (CP) modes available from the RADARSAT Constellation Mission (RCM). This work first uses the conventional semi-empirical Water Cloud Model (WCM) modified by exploiting the scattering power decompositions of CP measurements to estimate the Plant Area Index (PAI) for rice. The modified WCM (MWCM) is then inverted using the scattering power components from the $iS - \Omega$ decomposition. We compare the PAI estimates using MWCM- $iS - \Omega$ between the estimates obtained from (1) the conventional WCM using the RH and RV backscatter intensities and (2) MWCM- $m - \chi$ decomposition scattering powers. We exploit a time series of simulated compact-pol SAR data over the JECAM test site in Vijayawada, India, throughout 2018 and 2019. We use the C-band RADARSAT-2 full-pol data to simulate the RADARSAT Constellation Mission (RCM) compact-pol mode data. Utilizing the advantage of systematically collected multi-year SAR data and in-situ measurements, the present research also assesses the calibrated model transferability performances to another data set and cross-validation of a model in a multi-year experiment setting. The comparative analysis indicates potential improvements in PAI estimation with MWCM- $iS - \Omega$ scattering powers. A high range of correlation coefficient ($r = 0.84 \pm 0.06$) between the estimated and observed PAI is observed with good Root Mean Square Error (RMSE) of $0.778 \pm 0.107 \text{ m}^2 \text{ m}^{-2}$, and Mean Absolute Error (MAE) of $0.601 \pm 0.103 \text{ m}^2 \text{ m}^{-2}$.

ARTICLE HISTORY

Received 5 June 2021

Accepted 25 October 2021

CONTACT Dipankar Mandal  dipankar_mandal@iitb.ac.in  Microwave Remote Sensing Lab, Centre of Studies in Resources Engineering, Indian Institute of Technology Bombay, Mumbai, India

The multi-year cross-validation results also demonstrate the capability of transferring the calibrated model to another season with satisfactory performance for the PAI estimation.



1. Introduction

Active research is being pursued to evaluate the potential of the hybrid polarimetric architecture proposed by Raney (2007). Many are interested in using Compact Polarimetric Synthetic Aperture Radar (CP SAR) data for Earth observation monitoring. A hybrid-pol SAR system transmits either in a right circular (R) or a left circular (L) polarization and receives two coherent orthogonal linear polarizations, horizontal (H) and vertical (V). This mode is often termed as the Circular Transmit and Linear Receive (CTLR) (Raney 2007). CP SAR has an advantage over full-pol SAR systems in terms of a larger swath width but at the expense of added rich polarimetric information as compared to conventional dual-pol (Raney 2016; Touzi and Charbonneau 2014).

Several studies with CP SAR systems, e.g. RISAT-1 (Misra et al. 2013) and ALOS PALSAR-2 (Yokota et al. 2015), as well as simulated CP data from full-pol observations, have drawn considerable attention to the utility of CP data for earth observation applications. The Canadian RADARSAT Constellation Mission (RCM) provides data in CP mode (Thompson 2015). The RCM is a constellation of three identical C-band SAR satellites, which provide improved revisit opportunities. The performance of CP SAR data has been explored, comparing the information provided by this mode against that of dual and full polarimetric SAR data for different land features (Ainsworth, Kelly, and Lee 2009; Brisco et al. 2013; Charbonneau et al. 2010; Nord et al. 2009; Xie et al. 2015; Raney 2016; Ohki and Shimada 2018; Kumar et al. 2019; Mahdianpari et al. 2019). In particular, the potential of CP SAR data has been assessed for agricultural applications, including crop growth monitoring (Ballester-Berman and Lopez-Sanchez 2012; Shang et al. 2012; Lopez-Sanchez et al. 2014; Yang et al. 2014; Venkata et al. 2017; Kumar et al. 2017; McNairn et al. 2017; Homayouni et al. 2019), biophysical parameter retrieval (Yang, et al., 2016a; Zhang et al. 2017; Dave et al. 2017; Chauhan, Srivastava, and Patel 2018; Mandal et al. 2020) and soil moisture retrieval (Truong-Loi et al. 2009; Ouellette et al. 2014; Ponnurangam et al. 2016; Merzouki et al. 2019) using real as well as simulated CP SAR data.

In the context of crop biophysical parameter estimation, the semi-empirical Water Cloud Model (WCM) has been widely used due to its simplicity as well as effectiveness (Wigneron et al. 1999; Graham and Harris 2003). The WCM simulates SAR backscatter intensities in linear co- and cross-pol channels (i.e. in H-V basis) from a vegetation layer. This model has received significant attention for biophysical parameter estimation (Prevot, Champion, and Guyot 1993; De Roo et al. 2001; Inoue et al. 2002; Dabrowska-Zielinska et al. 2007; Kweon and Yisok 2015; Hosseini et al. 2015; Hosseini and McNairn 2017; Mandal et al. 2019c; Hosseini et al. 2021). However, limited studies have attempted the estimation of crop biophysical parameters with simulated compact-pol SAR data (Xie et al. 2015b; Zhang et al. 2017; Chauhan, Srivastava, and Patel 2018; Guo et al. 2018). Chauhan, Srivastava, and Patel (2018) used RISAT-1 hybrid-pol RH-RV intensities to estimate wheat leaf area index (LAI), plant water content (PWC), leaf water area index (LWAI) and interaction factor (IF) with high accuracy.

Among these crop descriptors, the LAI is the most commonly used crop growth monitoring using indirect measurement techniques, where it is not easy to distinguish between green and non-green elements, such as stems, shoots, and flowers (Jonckheere et al. 2004). Hence, an important source of error in indirect measurements comes from woody parts (e.g. branches and stems) that might be considered green vegetative

elements (Weiss et al. 2004). Therefore, alternative terms have been proposed in the literature, such as the 'Plant area index' (Neumann, Den Hartog, and Shaw 1989; Breda 2003). In plant physiology, PAI is expressed as a square metre of plant area per square metre ground. In the radar signal context, it is assumed that the scattering of EM waves is due to the interaction of all the vegetative parts of a crop canopy with radar signal. Hence, PAI is appropriate for SAR data analysis. However, LAI is defined as the one-sided leaf area per unit ground surface area. Thus, LAI, in general, is unable to compensate for the other canopy elements.

In the studies related to biophysical parameters with simulated compact-pol SAR, the conventional formulation of WCM is utilized, which accounts for the backscatter intensities in the linear-polarization (H-V) basis. However, the backscatter intensities are expressed in a circular basis, i.e. σ_{RH}° and σ_{RV}° . It is to be noted that in the CTR mode, the backscatter coefficients, σ_{RH}° and σ_{RV}° are proportional to $|HH + VH|^2$ and $|HV + WV|^2$, in which the co- and cross-polarized terms cannot be explicitly separated (Raney 2016). This impending characteristic compromises these experiments with the CTR mode while adopting the conventional formulation of WCM. Although a statistical transfer function derived between σ_{RH}° and σ_{HH}° , or σ_{RV}° and σ_{WV}° intensities could be an optimistic approach (Merzouki et al. 2019), indeed the cross-pol (σ_{HV}° or σ_{VH}°) component would increase errors for land targets where multiple or diffuse scattering contributes significantly to total scattering (Raney 2019; Lopez-Sanchez et al. 2014; Dey et al. 2020).

Apart from the backscatter intensity-based inversion approach, one may utilize a modified version of the WCM (Ulaby et al. 1984; Ulaby and Long 2015) to simulate scattering power components from vegetation canopy. Guo et al. (2018) utilized a modified WCM proposed by Yang et al. (2016b) to retrieve rice biophysical parameters from simulated CP SAR data. The modified WCM (MWCM) simulates scattering powers from distinct components of the vegetation-soil system. These scattering components are then associated with the three primary scattering power components obtained from the $m - \chi$ or the $m - \delta$ decompositions. The odd-bounce P_s , even-bounce P_d and diffuse P_v scattering power components from the $m - \chi$ and the $m - \delta$ decomposition represent the observed parameters. Crop parameters (e.g. Leaf Area Index – LAI, plant height, vegetation water content–VWC) are used as the target parameter in a genetic algorithm for MWCM inversion. The validation results reported a R^2 value of 0.64 and 0.70 and RMSE of 0.62 and $0.48\text{ m}^2\text{ m}^{-2}$ for $m - \chi$ and $m - \delta$ decompositions, respectively. These decompositions provide reasonable estimates for these crop biophysical parameters, where the scattering power components are derived only from the received backscattered information. The introduction of the polarized power fraction Ω (Bhattacharya et al. 2015) provides a wider degree of freedom by including transmit polarization information. This aspect helps accommodate a range of scattering mechanisms that are not exhibited in the existing decomposition techniques.

Hence, utilizing this polarization fraction parameter, Kumar et al. (2020) proposed an improvement in the scattering power components from the existing $S - \Omega$ decomposition (Bhattacharya et al. 2015). The improved $S - \Omega$ decomposition (called $iS - \Omega$) suitably takes care of the diffuse scattering powers, often overestimated by the $m - \chi$ and $m - \delta$ decompositions. The degree of dominance in the scattering-type from targets is attributed in $iS - \Omega$ to improve the scattering powers necessary for complete target



characterization. The new decomposition scattering power components may also improve the inversion accuracies of biophysical parameter estimation while utilizing them to relate with different scattering components of the vegetation-soil system in MWCM.

Despite these modelling approaches and their competitiveness, biophysical parameter retrieval with CP SAR using the WCM and its variants offers an opportunity to explore potential strategies with acceptable inversion accuracies. Moreover, the temporal robustness of model calibration and validation approaches are seldom investigated beyond specific calibration data sets. A framework for assessing cross-calibration and validation of different techniques with temporally rich data sets has not been fully explored (Beriaux et al. 2013; Hajj, Mohammad, and Zribi 2019). Such studies have been limited by the lack of large and diverse in-situ measurements collected coincident with SAR image acquisitions across diverse agro-ecosystems over multiple seasons (Beriaux et al. 2013). The JECAM SAR Inter-Comparison Experiment was designed to acquire such data sets over various global test sites (Dingle Robertson et al. 2017; Davidson et al. 2017; Hosseini et al. 2021). The JECAM SAR Inter-Comparison Experiment offers a platform to compare several inversion methodologies and conduct cross-validation experiments by ensuring consistency across the data sets. For these semi-empirical model-based inversion approaches, the framework for cross-calibration and validation requires a systematic investigation.

In this paper, the present research presents the following proposals:

- We propose to develop the best layout for model inversion while utilizing the backscatter coefficients in circular polarization RH-RV and scattering power components from decomposition techniques: $m - \chi$ or $iS - \Omega$ to retrieve the biophysical parameter of rice.
- We perform the model calibration and sensitivity analysis for a single season crop data.
- We assess the performances of the calibrated model transferability to other data sets while cross-validating a model in multi-year experiment settings.

2. Study area and data set

The test site is located in Vijayawada, India, as shown in Figure 1. This is the JECAM SAR test site in India (Mandal et al. 2017). The Vijayawada JECAM site covers the Krishna and Guntur districts in the state of Andhra Pradesh, India. The test site covers an area of approximately $50 \times 25 \text{ km}^2$ where rice is one of the major crops. Here, rice is grown in two distinct seasons: monsoon or *kharif* (June–November) and winter or *rabi* (December–March). A detailed description of the test site is provided in Mandal et al. (2019a).

2.1. In-situ measurements

We conducted the in-situ measurements during the Kharif season for two consecutive years: 2018 and 2019. In-situ measurements were available from the first week of June until November for both seasons, with approximately a revisit duration of 22 days. During the field campaigns, soil and crop information was collected over 75 agricultural fields, with a nominal size ranging from $60 \text{ m} \times 60 \text{ m}$ to $100 \text{ m} \times 100 \text{ m}$. In each sampling field,

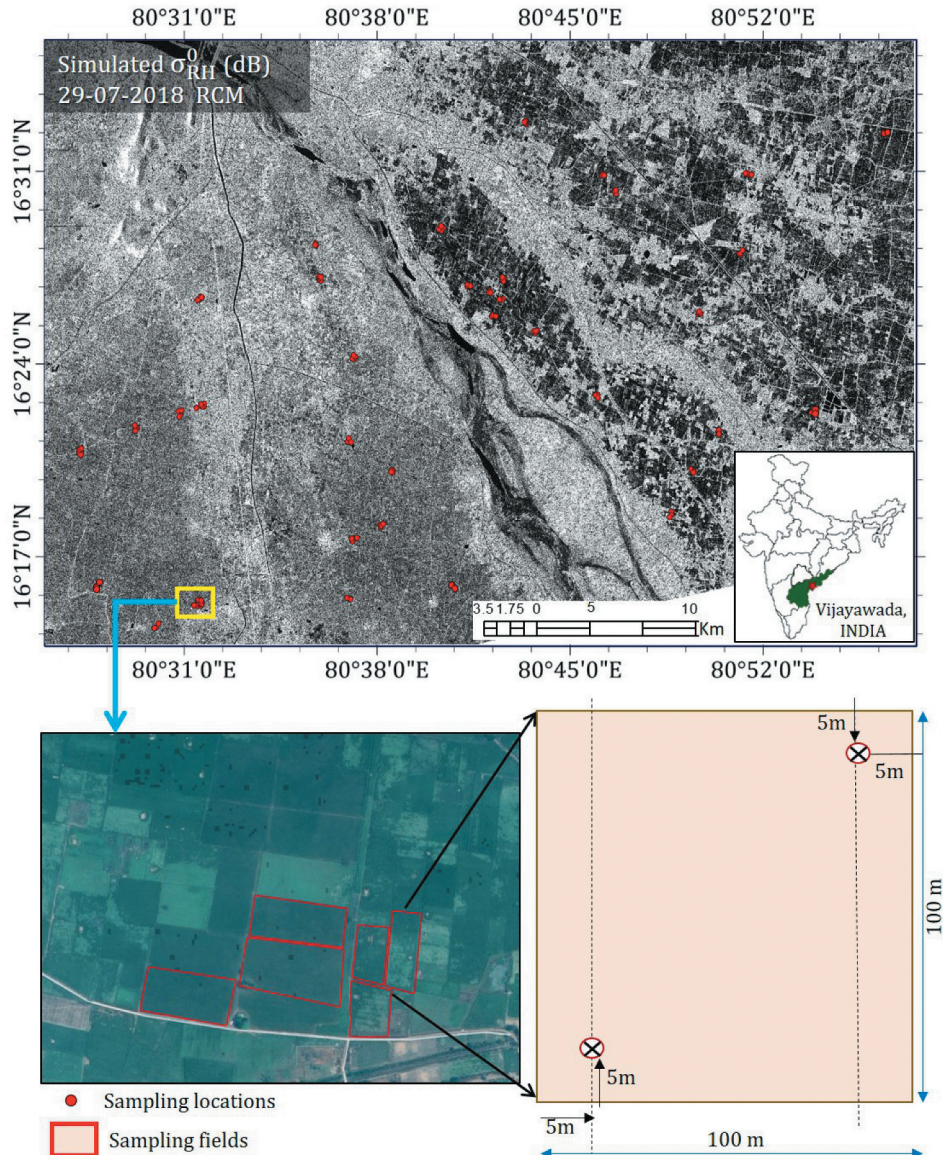


Figure 1. The JECAM-Vijayawada, India test site with a σ_{RH}^0 product simulated from RADARSAT-2 data of 29 July 2018. Locations of sampling sites are shown with red points. A layout of a sampling unit is also provided. Circles with a black cross inside refer to measurement points within each sampling field.

soil and crop measurements were recorded at two sampling locations, arranged in two parallel transects, as shown in Figure 1. We took soil moisture measurements at each sampling location using a theta-probe at 5 cm depth.

In each field, we conducted vegetation measurements at two points co-located with the soil sampling locations. It includes the measurement of plant area index (PAI) and phenology stages. During field sampling, we took 10 photographs along two transects separated by 2 m at each sampling point, using a wide-angle lens mounted on a digital



camera. All these images were post-processed using the CanEYE software (INRA 2017) to estimate PAI (Jonckheere et al. 2004; Weiss et al. 2004). Besides, we also measured wet biomass during the 2019 campaign by cutting rice plants above ground level. We utilized the biomass measurements and plant spacing information to derive the wet biomass per unit square metre area. The detailed description of vegetation and soil measurement strategies is documented in the field campaign report (Mandal et al. 2019a).

2.2. SAR dataset and preprocessing

During the Kharif season of each year, seven RADARSAT-2 images were acquired in Fine Quad Wide mode (FQW) over the test site, as given in Table 1. All acquisitions were in ascending orbit mode for 2018 and 2019 data sets with a scene centre incidence angle of 35.2°.

Several polarization combinations at varying spatial resolutions and noise floors (ranging from -25 dB to -17 dB) are available from RADARSAT Constellation Mission (Thompson 2015). Among these polarimetric products of RCM, the compact-pol (i.e. RH-RV) mode is of particular interest for land applications due to its large-scale attributes (Raney et al. 2021). In this present study, the CP datasets are simulated from full-pol RADARSAT-2 data (Table 1) using the compact-pol simulator in Sentinel-1 Toolbox 8.0 (ESA 2019) provided by SNAP with -24 dB of noise equivalent sigma zero (NESZ). The 2×2 covariance matrix \mathbf{C}_2 is generated for individual acquisitions. These \mathbf{C}_2 matrix elements are despeckled with the 3×3 refined Lee filter.

These multi-temporal images (elements of the \mathbf{C}_2) are then co-registered. Backscatter intensities σ_{RH}^o and σ_{RV}^o are first derived from the elements of the \mathbf{C}_2 matrix for individual dates followed by a geometric correction. The in-situ measurement points are then

Table 1. Specification of C-band full-pol RADARSAT-2 acquisitions over the test site during the field campaign. Field campaign windows for synchronous in-situ measurements are also included for reference.

Year	Acquisition date	Beam mode	Incidence angle range (deg.)	Orbit	In-situ measurements	Rice growth stages
2019	30 Jun	FQ15W	33.7–36.7	Ascending	29 June 1930 Jun, 01 Jul	Bare soil
	24 Jul	FQ15W	33.7–36.7	Ascending	23 July 2024 Jul, 25 Jul	Leaf development
	17 Aug	FQ15W	33.7–36.7	Ascending	16 August 2017 Aug	Early tillering
	10 Sep	FQ15W	33.7–36.7	Ascending	9 September 2010 Sep	Advanced tillering
	04 Oct	FQ15W	33.7–36.7	Ascending	3 October 2004 Oct	Booting
	28 Oct	FQ15W	33.7–36.7	Ascending	24 October 2025 Oct	Flowering
	21 Nov	FQ15W	33.7–36.7	Ascending	20 November 2021 Nov	Early to late dough
	05 Jul	FQ15W	33.7–36.7	Ascending	4 July 2005 Jul	Ploughed field
2018	29 Jul	FQ15W	33.7–36.7	Ascending	1 August 2002 Aug	Early tillering
	22 Aug	FQ15W	33.7–36.7	Ascending	22 August 2023 Aug	Advanced tillering
	15 Sep	FQ15W	33.7–36.7	Ascending	14 September 2015 Sep	Booting
	09 Oct	FQ15W	33.7–36.7	Ascending	8 October 2009 Oct	Flowering
	02 Nov	FQ15W	33.7–36.7	Ascending	2 November 2003 Nov	Early dough
	26 Nov	FQ15W	33.7–36.7	Ascending	25 November 2026 Nov	Maturity

overlaid on these $\sigma_{\text{RH}}^{\circ}$ and $\sigma_{\text{RV}}^{\circ}$ images. The backscattering intensities for each sampling location are calculated as the average over a 3×3 window centred on each site. Similarly, the polarimetric decomposition parameters are generated using the \mathbf{C}_2 elements, as described in Sec. 3.2.

3. Methodology

3.1. Vegetation modelling

In SAR theory, models to characterize vegetation canopy have evolved from classical physics-driven functions to semi-empirical forms to describe volume scattering from a continuous canopy layer (Graham and Harris 2003; Steele-Dunne et al. 2017). Simpler formulations of semi-empirical models, derived from the concept of the physics of scattering, have been extensively reviewed in the literature. Amongst these models, the Water Cloud Model (WCM) (Attema and Ulaby 1978) is widely used for the realization of scattering phenomena from a vegetation canopy. Attema and Ulaby (1978) originally formulated the model to characterize the total backscatter intensity (σ^0) in linear (H-V) polarization basis as,

$$\sigma^0 = AV_1^E \cos \theta \left(1 - \exp \left(-\frac{2BV_2^F}{\cos \theta} \right) \right) + (C' \times 10^{DM_v}) \times \exp \left(-\frac{2BV_2^F}{\cos \theta} \right) \quad (1)$$

where A, B, C', D, E , and F are the model coefficients and θ is the radar incidence angle. M_v represents the volumetric soil moisture. V_1 and V_2 are the plant canopy descriptors. In literature, different canopy descriptors are proposed to realize the vegetation canopy in WCM (Ulaby et al. 1984; Prevot, Champion, and Guyot 1993; Lievens and Verhoest 2011; Hosseini et al. 2015; Mandal et al. 2019c). In this study, we assess $V_1 = L$, $V_2 = L$, and $L = \text{PAI}$. It is important to note that in the case of rice cultivation, the underlying soil contains standing water or it close to saturation. Hence, the term DM_v can be suitably neglected. Subsequently, Eq. (2) is obtained from Eq. (1) as,

$$\sigma^0 = AL^E \cos \theta \left(1 - \exp \left(-\frac{2BL^F}{\cos \theta} \right) \right) + C \times \exp \left(-\frac{2BL^F}{\cos \theta} \right) \quad (2)$$

These models were initially developed to characterize radar intensities in linear polarization (H-V basis). However, more often, the expressions are directly adopted for the CTLR mode without any proper modification (Chauhan, Srivastava, and Patel 2017, 2018; Guo et al. 2018). It is to be noted that the backscatter intensities, $\sigma_{\text{RH}}^{\circ}$ and $\sigma_{\text{RV}}^{\circ}$ for CTLR mode are proportional to $|\text{HH} + \text{VH}|^2$ and $|\text{HV} + \text{VV}|^2$, in which the co- and cross-polarized terms cannot be explicitly separated (Raney 2016). However, in the present study, we utilize the original expression of WCM with $\sigma_{\text{RH}}^{\circ}$ and $\sigma_{\text{RV}}^{\circ}$ to compare it against a modified version of WCM, as addressed in the subsequent paragraphs.

Since the WCM is a semi-empirical model, it must be initially parameterized (i.e. calibrated) with in-situ measurements and corresponding backscatter intensities. The calibration step includes the estimation of model parameters (A, B, C, E and F) as expressed in Eq. (2). The model parameters are derived using the non-linear least square Levenberg-Marquardt algorithm (Moré 1978). The in-situ measured PAI and backscatter intensities (RH and RV) are then used to calibrate.

Subsequently, several modifications in the original form of WCM have been adapted to realize scattering phenomena from a vegetation canopy. They are generically referred to as the Modified Water Cloud Model (MWCM) in literature (Yang et al. 2016b; Xing et al. 2019). In the modified Water Cloud Model, the scattering powers are modelled within the crop canopy utilizing diverse scattering contributions from different layers (Ulaby et al. 1984; Yang et al. 2016b; Ulaby and Long 2015). Five scattering components are considered in this model, which includes:

- volume scattering from the rice tillers (V_{fr}),
- odd-bounce scattering from the leaf layer (S_t),
- odd-bounce scattering from the underlying standing water (S_{gt}),
- even-bounce scattering between tillers and underlying water surface (D_{tg}), and
- even-bounce scattering between the underlying water surface and tillers (D_{gt}).

The analytical expressions and their rationale can be obtained from (Ulaby et al. 1984; Ulaby and Long 2015; Yang et al. 2016b). These components are expressed as (3)–(7).

$$V_{fr} = (1 - F) \times A_{f1} \times (1 - \exp(-B_{f1}L)) \cos \theta \times (1 - \tau_{fr}^2(\theta)), \quad (3)$$

$$S_t = (1 - F) \times A_{t1} W \times \tau_{fr}^2(\theta), \quad (4)$$

$$S_{gt} = (1 - F) \times C_{g1}(\theta) M_v \times \tau_{fr}^2(\theta) \tau_t^2(\theta), \quad (5)$$

$$D_{tg} = A_{f2} \times (1 - \exp(-B_{f2}L)) \times F \times C_{g2}(\theta) M_v \times \tau_{fr}^2(\theta), \quad (6)$$

$$D_{gt} = F \times C_{g2}(\theta) M_v \times A_{t2} W \times \tau_{fr}^2(\theta), \quad (7)$$

where, L , W , and M_v are Plant Area Index (PAI), wet biomass, and volumetric soil moisture, respectively, and θ is the radar incident angle. The attenuation factors are expressed as:

$$\tau_{fr}^2(\theta) = \exp(-2a_f L \sec \theta), \quad (8)$$

$$\tau_t^2(\theta) = \exp(-2a_t W \sec \theta). \quad (9)$$

The parameters A_{f1} , B_{f1} , A_{t1} , $C_{g1}(\theta)$, B_{f2} , $C_{g2}(\theta)$, and A_{t2} , a_f , a_t along with F are characterized as model coefficients. Here, it is important to note that due to the presence of standing water in rice fields, the volumetric soil moisture, M_v , is omitted while replacing it with the Fresnel coefficient of water (≈ 1.0). Here, one can note that rice fields during the maturation stages are generally not flooded, and the senescence of plants starts from the bottom to the top. Hence, the contribution from the soil moisture cannot be neglected *a priori*. However, the field conditions and precipitation events during the maturity stages over the JECAM-India test site reasonably allows us to consider *a priori* elimination of the soil contribution. Under such fields conditions (i.e. fields fully saturated due to heavy rain), the contribution from the matured rice canopy (although dried as senescence started but vegetation water content is potentially increased due to rain events) is much more significant than the soil. Nevertheless, one cannot guarantee that such conditions are always full-filled for other test sites. Hence, caution should be exercised while considering such *a priori* information.

In this study, the wet biomass measurements are only available for 2019 data sets. Hence, a regression model between PAI and wet biomass (Appendix A), which is derived from 2019 data sets, is utilized for data sets from 2018 as a proxy to wet biomass.

We obtain the model coefficients by fitting both the in-situ measurements from the canopy and SAR observables. Instead of the backscatter intensities (σ_{RH}^o and σ_{RV}^o), the scattering power components (i.e. P_v , P_s , and P_d) from rice canopy are utilized in this study (Yang et al. 2016b):

$$\begin{bmatrix} P_v \\ P_s \\ P_d \end{bmatrix} = \begin{bmatrix} V_{fr} \\ S_t + S_{gt} \\ D_{tg} + D_{gt} \end{bmatrix} \quad (10)$$

A detailed description of these scattering powers derived for CP SAR data is provided in Sec. 3.2.

3.2. Scattering power decomposition

In general, scattering power decompositions for CP SAR data are expressed in terms of the even-bounce, odd-bounce, and diffuse scattering power components (Raney 2007; Keith et al. 2012; Cloude, Goodenough, and Chen 2012). For the CTR mode, the received signal can be presented in terms of four real elements of the Stokes vector (S_{r0} , S_{r1} , S_{r2} , S_{r3}). This Stokes vector is formed from the 2×2 covariance \mathbf{C}_2 matrix as (11):

$$\begin{bmatrix} S_{r0} \\ S_{r1} \\ S_{r2} \\ S_{r3} \end{bmatrix} = \begin{bmatrix} C_{11} + C_{22} \\ C_{11} - C_{22} \\ C_{12} + C_{12}^* \\ \pm j(C_{12} - C_{12}^*) \end{bmatrix} \quad (11)$$

Scattering phenomena in compact-pol SAR mode are usually characterized by the secondary/child Stokes parameters, such as the degree of polarization (m), and the received ellipticity (χ) or the degree of circularity ($\sin 2\chi$). These parameters are derived from the Stokes vector as given in (12) and (13):

$$m = \frac{\sqrt{S_{r1}^2 + S_{r2}^2 + S_{r3}^2}}{S_{r0}}, \quad 0 \leq m \leq 1, \quad (12)$$

$$\chi = \frac{1}{2} \sin^{-1} \left(\pm \frac{S_{r3}}{m S_{r0}} \right), \quad -45^\circ \leq \chi \leq +45^\circ. \quad (13)$$

These parameters form the basis of the $m - \chi$ scattering power decomposition in CP SAR theory (Keith et al. 2012). The degree of polarization, m , is an essential parameter characterizing partially polarized electromagnetic waves and is closely related to entropy (Aiello and Woerdman 2005). The sign of χ indicates the handedness of the received polarization ellipse. A target decomposition technique essentially divides the total back-scattering power (S_{r0}) into three primary constituents: odd-bounce (i.e. Bragg and specular) P_s , even-bounce (i.e. dihedrals and diplanes) P_d , and diffuse (randomly polarized) P_v . The $m - \chi$ decomposition characterizes the scattering power distribution from a target as expressed in (14).

$$\begin{bmatrix} P_v \\ P_s \\ P_d \end{bmatrix}_{m-\chi} = \begin{bmatrix} S_{r0}(1-m) \\ mS_{r0}(1+\sin 2\chi)/2 \\ mS_{r0}(1-\sin 2\chi)/2 \end{bmatrix} \quad (14)$$

The $m - \chi$ decomposition considers two among the three primary components (m, χ, ψ) that are required to describe the polarized part of the quasi-monochromatic partially polarized wave. Among these three parameters, ψ indicates the orientation of the polarization ellipse in the backscattered field (Raney 2016).

In a recent study, Kumar et al. (2020) improved the scattering power components utilizing the proposed $iS - \Omega$ decomposition. It uses the ratio of the power received in the same-sense circular ($SC = (S_{r0} - S_{r3})/2$) and opposite-sense circular ($OC = (S_{r0} + S_{r3})/2$) polarization echo (SC/OC) as a criterion for scattering dominance in $iS - \Omega$. The $iS - \Omega$ decomposition suitably redistributes the scattering powers in odd and even-bounce components depending on the CPR and utilizes the polarized power fraction (Ω) and SC and/or OC for power estimates.

For $SC/OC < 1$, i.e. the odd-bounce (P_s) scattering power component is dominant, while the even-bounce (P_d) scattering power component is non-dominant. Consequently, from the total polarized power, ΩS_{r0} , the non-dominant scattering power is first obtained by suppressing the SC power component with the unpolarized power fraction ($1 - \Omega$). This component is then modulated with Ω to obtain the even-bounce scattering power, i.e. $P_d = \Omega(1 - \Omega)SC$. Therefore, the residual power corresponds to the dominant odd-bounce scattering power component. It is obtained by subtracting the P_d power from the total polarized power, i.e. $P_s = \Omega S_{r0} - \Omega(1 - \Omega)SC$. Similarly, a vice-versa approach is applied when considering $SC/OC > 1$, i.e. calculating the dominant even-bounce scattering power. The diffuse scattering power, P_v is obtained by multiplying S_{r0} with the unpolarized power fraction ($1 - \Omega$).

3.3. Experiment design for PAI estimation

In this research, we focus on the retrieval of PAI of rice using the Modified WCM. We invert the MWCM utilizing the observed scattering powers from the $iS - \Omega$ decomposition to estimate the biophysical parameters. Besides, we compare the proposed method for PAI estimation with the existing workflow to invert the WCM utilizing the backscatter intensities (σ_{RH}^o and σ_{RV}^o) as given in (2). We parametrize the models (viz., WCM, and MWCM) with the same calibration dataset, primarily as a fundamental first step. We formulate the MWCM with scattering powers obtained from 1) $m - \chi$ and 2) $iS - \Omega$ decompositions. For rice biophysical parameter estimation, the five scattering components in the formulation of the MWCM are equated with scattering power components of $iS - \Omega$ and $m - \chi$, as Eq. (15) and (16). We divide the sample data in a 60:40 ratio for calibration and validation purposes. A schematic workflow of this experiment is shown in Figure 2.

$$\begin{bmatrix} P_v \\ P_s \\ P_d \end{bmatrix}_{m-\chi} = \begin{bmatrix} V_{fr} \\ S_t + S_{gt} \\ D_{tg} + D_{gt} \end{bmatrix} \quad (15)$$

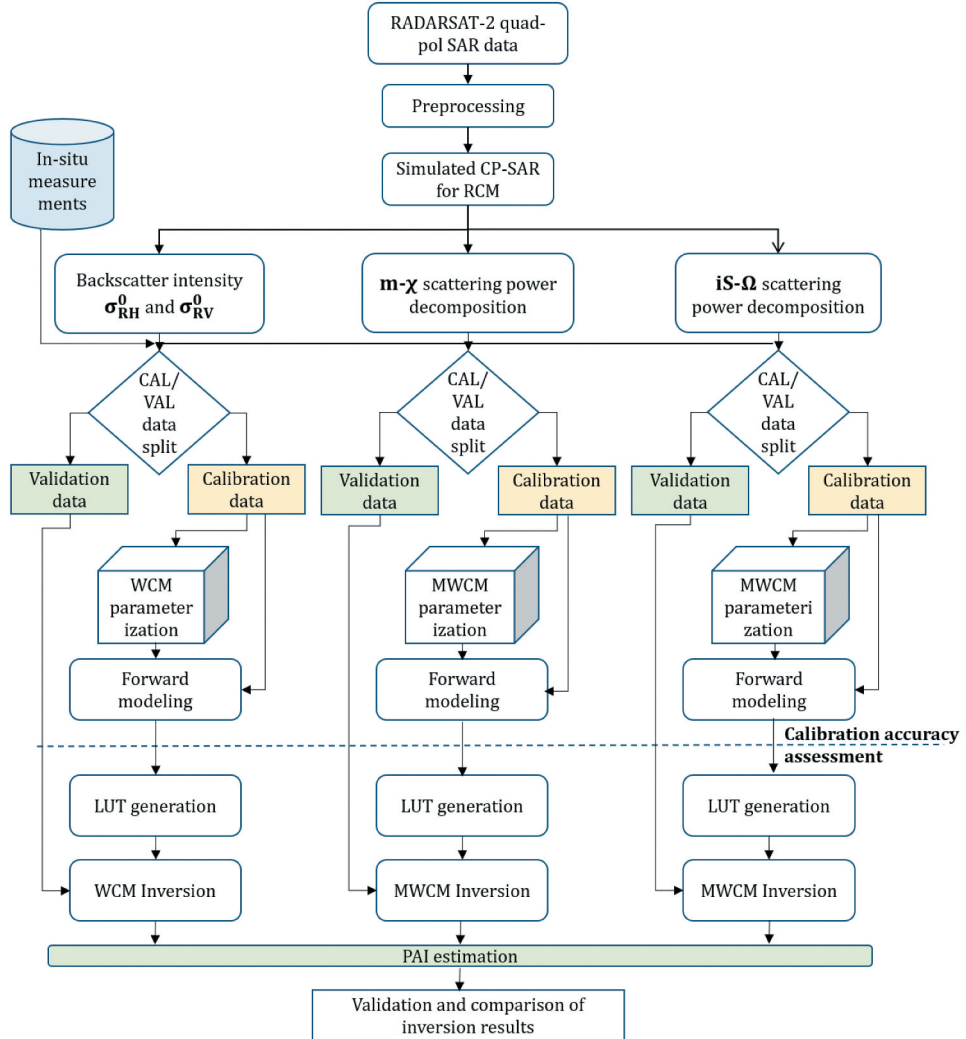


Figure 2. Schematic workflow of the experiment settings for cross-validation strategies to estimate PAI using WCM and MWCM.

$$\begin{bmatrix} P_V \\ P_s \\ P_d \end{bmatrix}_{is-\Omega} = \begin{bmatrix} V_{fr} \\ S_t + S_{gt} \\ D_{tg} + D_{gt} \end{bmatrix} \quad (16)$$

We first compare the calibration results with the observed SAR responses to evaluate the suitability of these vegetation models. We use the correlation coefficient (r) between the observed and estimated parameters as a metric to assess the performance of these models. We evaluate the accuracies between the observed and the estimated radar parameters for the calibration dataset with the RMSE.

Given the multi-year cross-calibration study, we split the data sets from 2019 and 2018 to generate several subsets. The data subsets are generated based on several criteria imposed on PAI ranges and rainfall events, as presented in [Table 2](#).



It is important to note that the estimation of PAI from these semi-empirical models (WCM and MWCM) is often recognized as an ill-posed inversion problem (Bériaux et al. 2015; Mandal et al. 2019b). The ill-posed inversion problems of PAI retrieval are achieved using the Look-up Table (LUT) search approach. In this process, first, we simulate the backscatter intensities in both polarizations (i.e. RH and RV) for the forward modelling of the WCM for a combination of vegetation parameters from the calibration data. Similarly, we simulate the scattering powers from the $m - \chi$ and $iS - \Omega$ decompositions with the calibration dataset to form the LUT.

We use the validation dataset to estimate the PAI by searching this LUT. For a given set of backscatter intensities (e.g. values at RH and RV polarization), the inverse problem seeks to find the crop parameters. To select the solution of the inverse problem, the LUT is sorted according to a cost function (e.g. root mean square error; RMSE). The error function with the backscatter intensity values at each polarization (RH and RV) are calculated as

$$\text{RMSE} = \sqrt{\frac{1}{2} \left((\sigma_{\text{RH}}^{\text{observed}} - \sigma_{\text{RH}}^{\text{LUT}})^2 + (\sigma_{\text{RV}}^{\text{observed}} - \sigma_{\text{RV}}^{\text{LUT}})^2 \right)} \quad (17)$$

The solution is considered at the configuration, which provides the minimum RMSE value (Mandal, Bhattacharya, and Rao 2021). A similar approach is considered for decomposition power-based approaches.

Finally, we compare the PAI inversion results with these three test cases, i.e. WCM, MWCM with $m - \chi$, and MWCM with $iS - \Omega$. The retrieval accuracies are compared in terms of correlation coefficient (r), RMSE, and Mean Absolute Error (MAE) between the observed and estimated PAI using the validation dataset. We also analyse the temporal robustness of the model calibration and validation by considering several calibration data subsets while validating the PAI retrieval results with all the other cases.

4. Results and discussion

In this study, we perform six different calibrations by splitting the data set according to all possible combinations of observation data from 2018 and 2019 and specific criteria (Table 2). These six different data sets are used to calibrate both the WCM and MWCM. Subsequently, we perform cross-validation experiments for single and multi-year cases. For the ease of understanding for the readers, we discuss the single-year and multi-year cross-validation results separately in Sec. 4.1, 4.2, 4.3.

4.1. Analysis of 2019 data set

4.1.1. Model sensitivity analysis

Here, we have performed the parameterization of the WCM and MWCMs using the calibration data sets. Moreover, we assess the use of $\sigma_{\text{RH}}^{\circ}$ and $\sigma_{\text{RV}}^{\circ}$ in the WCM, which is often ambiguously adopted in several studies (Chauhan, Srivastava, and Patel 2017, 2018). These studies utilize the conventional formulation of WCM, which was originally developed to account for the backscatter intensities in the linear-polarization (H-V) basis, i.e. HH, VV, and HV or VH. However, these expressions have been directly adopted for the CTR mode without any modifications. There is no physical basis for adopting such a

Table 2. Specification of data subsets for CAL/VAL cross-validation experiments using 2019 and 2018 data sets.

Experiment	Year	Criteria for data subset	
		Calibration	Validation
Single year experiments:			
CAL19-1/ VAL19-1	CAL19-1: 2019 VAL19-1: 2019	All data having full range of PAI between [0, 8]	All data having full range of PAI between [0, 8]
CAL19-1/ VAL19-2	CAL19-1: 2019 VAL19-2: 2019	All data having full range of PAI between [0, 8]	All data having range of PAI between [0, 4.5], PAI>4.5 = = NaN
CAL19-2/ VAL19-2	CAL19-2: 2019 VAL19-2: 2019	All data having range of PAI between [0, 4.5]	All data having range of PAI between [0, 4.5], PAI>4.5 = = NaN
CAL19-3/ VAL19-2	CAL19-3: 2019 VAL19-2: 2019	All data having range of PAI between [0, 4.5] & exclude data from precipitation events	All data having range of PAI between [0, 4.5], PAI>4.5 = = NaN
CAL18-1/ VAL18-1	CAL18-1: 2018 VAL18-1: 2018	All data having full range of PAI between [0, 8]	All data having full range of PAI between [0, 8]
CAL18-1/ VAL18-2	CAL18-1: 2018 VAL18-2: 2018	All data having full range of PAI between [0, 8]	All data having range of PAI between [0, 4.5], PAI>4.5 = = NaN
CAL18-2/ VAL18-2	CAL18-2: 2018 VAL18-2: 2018	All data having range of PAI between [0, 4.5]	All data having range of PAI between [0, 4.5], PAI>4.5 = = NaN
Multi-year experiments:			
CAL18-2/ VAL19-2	CAL18-2: 2018 VAL19-2: 2019	All data having range of PAI between [0, 4.5]	All data having range of PAI between [0, 4.5], PAI>4.5 = = NaN
CAL19-2/ VAL18-2	CAL19-2: 2019 VAL18-2: 2018	All data having range of PAI between [0, 4.5]	All data having range of PAI between [0, 4.5], PAI>4.5 = = NaN
CAL19-3/ VAL18-2	CAL19-3: 2019 VAL18-2: 2018	All data having range of PAI between [0, 4.5] & exclude data from precipitation events	All data having range of PAI between [0, 4.5], PAI>4.5 = = NaN
CAL1918/ VAL18-2	CAL1918: 2019 & 2018 VAL18-2: 2018	All data having range of PAI between [0, 4.5] & exclude data from precipitation events	All data having range of PAI between [0, 4.5], PAI>4.5 = = NaN
CAL1918/ VAL19-2	CAL1918: 2019 & 2018 VAL19-2: 2018	All data having range of PAI between [0, 4.5] & exclude data from precipitation events	All data having range of PAI between [0, 4.5], PAI>4.5 = = NaN

(Continued)

**Table 2.** (Continued).

Experiment	Year	Criteria for data subset	
		Calibration	Validation
Single year experiments:			
	VAL19-2: 2019		
CAL1918/ VAL1918	CAL1918: 2019 & 2018 VAL1918: 2019 & 2018	All data having range of PAI between [0, 4.5] & exclude data from precipitation events	All data having range of PAI between [0, 4.5], PAI>4.5 = = NaN

linear basis WCM model for CTR mode. In these studies, the WCM is also initially parameterized independently for both RH and RV backscatter intensities. Besides, we evaluate the accuracies of the calibrated WCMs by comparing the observed and simulated backscatter intensities. The results are evaluated in terms of the correlation coefficient (r), the Root Mean Square Error (RMSE), as given in [Table 3](#). It is important to note that the backscatter intensities are utilized in a linear scale for WCM parameterization. However, we assess the accuracies of the calibrated WCMs by comparing the observed and simulated backscatter intensities in the decibel (dB) scale.

The correlation coefficients (r) between the observed and simulated backscatter intensities are 0.63 (RH) and 0.62 (RV), considering the full range of PAI in the calibration data set (CAL19-1) with an RMSE of ≈ 1.69 dB. However, we notice improvements in accuracy while using scattering power decomposition elements in the MWCMs. The accuracies of the calibrated MWCMs are evaluated between the observed and simulated scattering powers (P_v , P_s , and P_d) for both $m - \chi$ and $iS - \Omega$ decomposition. For the $m - \chi$ decomposition, the correlation coefficients (r) between the observed and estimated scattering powers are 0.73 (P_v), 0.70 (P_s), and 0.70 (P_d). The RMSE is lowest for P_v (1.41 dB) as compared to P_s , and P_d powers (1.45 and 1.47 dB, respectively). The P_v power is sensitive to canopy growth due to diffuse scattering within the plant canopy. The depolarization of the electromagnetic wave is apparent due to multiple scattering events, which reduces the degree of polarization (m). Moreover, the simulated even-bounce scattering power, P_d , corresponds well with the observed data. In this case, the interaction of the incident wave with the vertical stems, erectophile leaves, and the underlying standing water leads to the dominance of the even-bounce scattering mechanism (Wang et al. [2009](#); Le Toan et al. [1997](#)).

The simulated $iS - \Omega$ decomposition parameters from the MWCM better correlate with the observed scattering powers when compared to the results from $m - \chi$, in the case of CAL19-1. Incorporating the degree of dominance in the scattering mechanism (i.e. using the circular polarization ratio (CPR) as a criterion for scattering dominance) in the $iS - \Omega$ decomposition improve the scattering powers decomposition. For the $iS - \Omega$ decomposition parameters, the correlation coefficients (r) between the observed and estimated scattering powers are 0.75 (P_v), 0.73 (P_s), and 0.71 (P_d). The RMSE is lowest (1.36 dB) for P_v as compared to P_s , and P_d (1.40 dB and 1.41 dB, respectively).

Table 3. Error estimates of the WCM (RH and RV) and the MWCM ($m - \chi$ and $iS - \Omega$ scattering powers) using different calibration data sets from multi-year observations.

Year	Calibration data set	Statistics	WCM			MWCM: $m - \chi$			MWCM: $iS - \Omega$		
			RH	RV	Pv	Ps	Pd	Pv	Ps	Pd	
2019	CAL19-1 (n ¹ = 50)	r	0.63	0.62	0.73	0.70	0.70	0.75	0.73	0.71	
		RMSE ²	1.69	1.70	1.41	1.45	1.47	1.36	1.40	1.41	
	CAL19-2 (n = 42)	r	0.66	0.68	0.75	0.74	0.71	0.78	0.75	0.74	
		RMSE	1.52	1.50	1.36	1.43	1.48	1.29	1.36	1.43	
	CAL19-3 (n = 36)	r	0.68	0.70	0.76	0.74	0.75	0.80	0.76	0.76	
		RMSE	1.48	1.46	1.31	1.35	1.42	1.20	1.31	1.40	
2018	CAL18-1 (n = 150)	r	0.65	0.61	0.71	0.68	0.64	0.75	0.73	0.71	
		RMSE	1.68	1.78	1.50	1.53	1.58	1.35	1.37	1.46	
	CAL18-2 (n = 144)	r	0.65	0.66	0.78	0.72	0.73	0.82	0.80	0.78	
		RMSE	1.56	1.52	1.41	1.46	1.50	1.21	1.26	1.35	
2019 & 2018	CAL1918 (n = 180)	r	0.64	0.68	0.75	0.72	0.76	0.83	0.82	0.81	
		RMSE	1.60	1.58	1.37	1.48	1.55	1.22	1.31	1.36	

¹n is number of observations points.

²The RMSE of the calibrated WCM and MWCMs are assessed by comparing the observed and simulated backscattered powers in the decibel (dB) scale.

It is interesting to note that the error estimates decrease for CAL19-2 and CAL19-3 irrespective of vegetation models (Table 3). Considering the saturation of radar response at C-band and high vegetation cover (PAI $> 4.5 \text{ m}^2 \text{ m}^{-2}$), exclusion of high PAI values in the calibration data provided a better fit to model (CAL19-2). Indeed, the calibration data, excluding SAR observations during rainfall events (CAL19-3), provided the best fit to WCM and MWCM in terms of r and RMSE values. For a better understanding of these results for several calibration models of 2019, we present sensitivity plots in Figure 3. These plots provide the simulated backscatter intensities and scattering powers as a function of PAI for saturated soil conditions. The incidence angles considered in each simulation, as shown in Figure 3 are equal to the mean incidence angle of the RADARSAT-2 data acquired over the region.

For WCM simulations, the green lines represent vegetation backscatter coefficient ($\sigma_{\text{veg}}^{\circ}$), while the brown lines represent the backscattering coefficient from the soil attenuated by the vegetation ($\tau^2 \sigma_{\text{soil}}^{\circ}$). The black lines represent the total backscatter coefficient ($\sigma_{\text{total}}^{\circ}$) for the soil-vegetation system with saturated soils. On the other hand, for MWCM simulations, blue, red, and light-green lines represent P_s , P_d , and P_v scattering powers, respectively.

Simulated results from CAL19-1 and CAL19-2 models indicate the differential sensitivity of all components in the WCM and MWCM, which arises principally considering the full range of PAI values during model calibrations. While considering the full range of PAI (0–8 $\text{m}^2 \text{ m}^{-2}$) data sets (CAL19-1) during model calibration, the radar observables at higher PAI values ($> 4.5 \text{ m}^2 \text{ m}^{-2}$) are likely to be affected by saturation of the radar signal while being insensitive to changes in PAI. These data sets affect the curve fitting results during calibration of the WCM and MWCM.

For the $\sigma_{\text{RH}}^{\circ}$ model in CAL19-1, the attenuated soil component contributes more significantly to total backscatter than vegetation with a range between –15 dB to –11 dB for PAI $< 4.5 \text{ m}^2 \text{ m}^{-2}$. Vegetation contribution is considerably lower within a range of –40 dB to –20 dB. The $\sigma_{\text{RH}}^{\circ}$ is mostly affected by the underlying soil surface

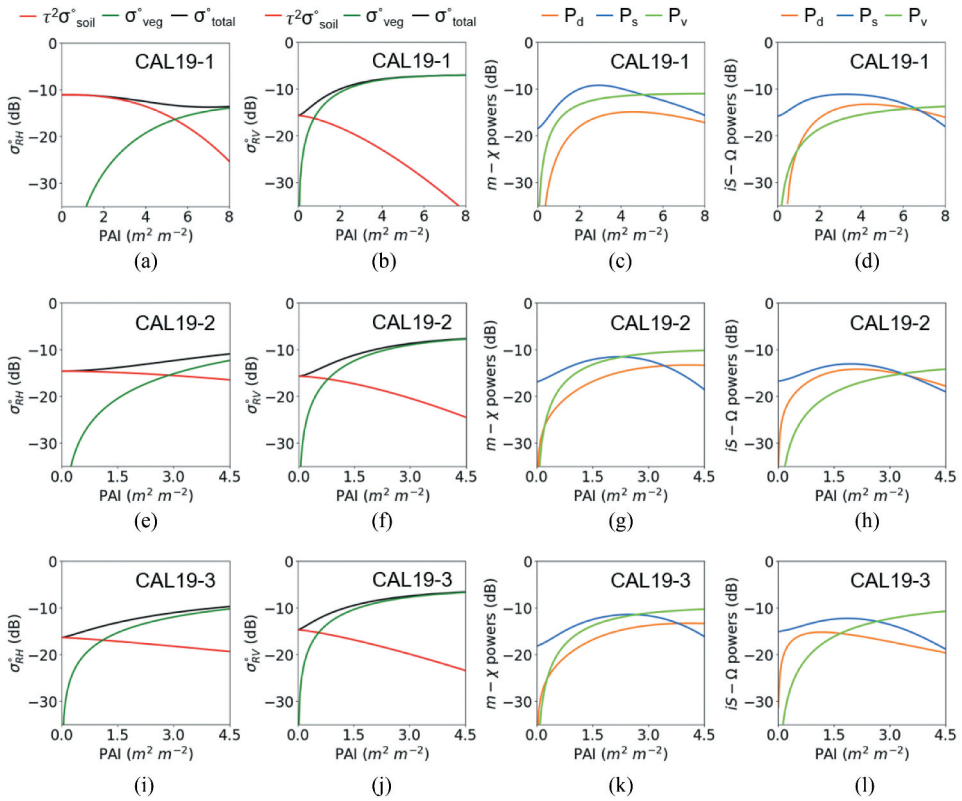


Figure 3. Simulations of backscatter powers with varying PAI ranges for WCM (σ_{RH}° and σ_{RV}°) and MWCMs ($m - \chi$ and $iS - \Omega$ decomposition powers) parameterized with different calibration data subsets pooled from observations of 2019. Simulated parameters for (a-d) CAL19-1, (e-h) CAL19-2, and (i-l) CAL19-3 data subsets.

(Kumar et al. 2017). Although at higher PAI values, the σ_{veg}° contribution is larger than $\tau^2\sigma_{soil}^{\circ}$. The $\tau^2\sigma_{soil}^{\circ}$ contribution reduced in a nonlinear decay rate. On the contrary, the variation in $\tau^2\sigma_{soil}^{\circ}$ changes almost linearly in the CAL19-2 model of σ_{RH}° .

We observe a differential sensitivity of σ_{total}° in σ_{RH}° , when the WCM is calibrated with CAL19-1 and CAL19-2 data sets. As compared to σ_{RH}° , the differential sensitivity between CAL19-1 and CAL19-2 is less pronounced in the case of σ_{RV}° , except for a change in the steepness of the σ_{veg}° curves within the PAI ranges. The differential behaviour of RH and RV is apparent due to the dominant vertical structure of the rice stem and the erectophile leaf distribution. This sensitivity can be related to the geometry of the crop. Rice having an erectophile canopy, the scattered H signal is primarily affected due to the underlying soil surface rather than the plant. Indeed, the scattered H wave is attenuated by the vegetation. On the other hand, the V signal is mainly affected due to the interaction of the vertically polarized wave with the vertical plant components (Lopez-Sanchez et al. 2014). It is important to note here that the saturation of σ_{total}° in RV at higher PAI values is likely due to the attenuation of the C-band signal within the rice canopy.

We observe differences in power values with changes in PAI for the CAL19-1 and CAL19-2 model while considering the MWCM model parameters in $m - \chi$ and $iS - \Omega$. At low PAI values ($< 1.5 \text{ m}^2 \text{ m}^{-2}$), the dominance of odd-bounce (P_s) scattering is apparent from both the decomposition techniques ($m - \chi$ and $iS - \Omega$) irrespective of CAL19-1 and CAL19-2 data sets. When we compare the decomposition methods, an increase of 11% is observed in the P_s power for $iS - \Omega$ compared to the $m - \chi$ decomposition. On the contrary, the diffuse scattering power reduces by $\approx 12\%$ for the $iS - \Omega$ decomposition. Overestimation of the diffused scattering power in $m - \chi$ decomposition was also reported by Kumar et al. (2020) with an experiment over corner reflectors.

With increased PAI at advanced tillering stages, the even-bounce scattering increased significantly in the case of $iS - \Omega$. This behaviour is likely due to the interaction of the EM wave with the vertical stems, erectophile leaves, and the flooded surface condition, leading to an even-bounce scattering mechanism (Wang et al. 2009; Le Toan et al. 1997). During the tillering stage of rice, the dominance of even-bounce scattering was also reported with simulated compact-pol data from C-band RADARSAT-2 observations (Lopez-Sanchez et al. 2014). With a subsequent increase in PAI, the contribution from even-bounce power reduces with the increase in the diffuse scattering power. However, the dynamic ranges of scattering powers are different in $m - \chi$ and $iS - \Omega$ irrespective of the calibration models.

The $iS - \Omega$ suitably redistributes the scattering powers in odd and even bounce components depending on the circular polarization ratio (CPR = SC/OC). The hierarchical nature of the $iS - \Omega$ decomposition introduces a measure of dominancy via the CPR parameter wherein the non-dominant scattering power is suppressed by the unpolarized fraction ($1 - \Omega$). The dominant power is then calculated by differencing the non-dominant component from the polarized part of the total power ($\Omega \times S_{r0}$). For $SC/OC < 1$, i.e. the dominant part is the odd bounce scattering, and the non-dominant part is the even bounce scattering. From the total polarized power ($\Omega \times S_{r0}$), the non-dominant scattering power is obtained first by suppressing the SC power with the unpolarized factor ($1 - \Omega$) and then modulating it with Ω to get $P_d = \Omega \times SC \times (1 - \Omega)$. The resultant remaining power corresponds to the dominant power, i.e. the odd bounce scattering and is obtained by subtracting the P_d power from the total polarized power as $P_s = \Omega \times S_{r0} - (\Omega \times SC \times (1 - \Omega))$ or simplified as $P_s = \Omega \times (S_{r0} - SC \times (1 - \Omega))$. A similar vice-versa approach is applied when $SC/OC > 1$, i.e. to calculate the dominant even bounce scattering power. However, in the existing compact-pol decompositions such as $m - \chi$, the unpolarized part, ($1 - m$) of the received wave, is considered volume scattering. In contrast, the odd and the even bounce scattering is formulated by geometric factors ($1 \pm \sin 2\chi$ to modulate half of the total polarized power ($mS_0/2$)). In an experiment with pure or elementary targets (triangular and dihedral corner reflectors), Kumar et al. (2020) showed that $m - \chi$ suppresses the double bounce. The portion of it shifts to the volume component. However, $iS - \Omega$ indeed indicated a better estimate of the double-bounce power. So, during crop growth stages, $iS - \Omega$ powers are more reliable than $m - \chi$.

Here, it is important to note that the measured backscatter intensities and the scattering powers at some pixels are close to the NESZ (the NESZ of the simulated RCM products is ≈ -24 dB, much higher than the -35 dB of full-pol RADARSAT-2 in Fine-Quad mode).

Consequently, the estimation of these polarimetric observables would be affected by noise. Hence, the interpretation of scattering powers below -24 dB would be compromised.

It is interesting to observe the effect of rain events on model calibration. The CAL19-3 data set excludes the acquisition from rainfall events. These data sets have different distributions of SAR observables, and thereby their sensitivity is different relative to CAL19-2 for all cases of the WCM and MWCM (Figure 3). The error estimates indicate that CAL19-3 has the lowest RMSE and would significantly impact the validation process. It is well understood that rain influences SAR signal transmission and the backscatter response. Thus, we exclude data acquired during a rainfall event in several experiments. Typically, we include SAR data obtained during rainfall in some calibration models to measure the significance of its impact.

4.1.2. Validation of PAI estimates

We perform cross-validation with the calibration models and validation data sets for retrieval of PAI. The calibrated model (WCM and MWCM) is first used to generate LUT by a forward modelling approach followed by PAI estimation with in-situ validation data sets. Hence, each CAL/VAL data combination is used for cross-validation, as shown in Figure 4. We compare the estimated PAI with the in-situ measurements on a 1:1 plot to assess the retrieval performance of each model (WCM and MWCM) using the validation data. We perform comparisons using the correlation coefficient (r), RMSE, and mean absolute error (MAE). The validation of PAI estimates for each case (CAL/VAL) is conducted for the inversion based on three models: 1) WCM based on σ_{RH}^o and σ_{RV}^o , 2) MWCM based on $m - \chi$ scattering power decomposition, and 3) MWCM based on $iS - \Omega$ scattering power decomposition.

The cross-validation experiment sets with 2019 data provide promising results for PAI estimates with RMSE varying from 0.672 to $1.031\text{ m}^2\text{ m}^{-2}$ and MAE varying from 0.515 to $0.765\text{ m}^2\text{ m}^{-2}$. Among these four CAL/VAL experiments, highest error rates are observed when we have utilized the full range of PAI for calibration and validation (CAL19-1/VAL19-1) for three estimation options ($\sigma_{RH}^o - \sigma_{RV}^o$, $m - \chi$, and $iS - \Omega$). The correlations between observed and estimated PAI values are improved when PAI ranges are restricted between 0 and $4.5\text{ m}^2\text{ m}^{-2}$ in the validation data (VAL19-2). It also reduced the error estimates by 5–13% for the $\sigma_{RH}^o - \sigma_{RV}^o$, $m - \chi$, and $iS - \Omega$ based retrievals.

When we limited the range of PAI between 0 and $4.5\text{ m}^2\text{ m}^{-2}$ for both the calibration and validation data (CAL19-2/VAL19-2), the error rates got further reduced significantly. The correlation between the observed and estimated PAI values also got improved for all three cases with r of 0.67 ($\sigma_{RH}^o - \sigma_{RV}^o$), 0.79 ($m - \chi$), and 0.82 ($iS - \Omega$). Comparing the PAI retrieval options, we find that the highest errors are reported for RH-RV with $\text{RMSE} = 0.894\text{ m}^2\text{ m}^{-2}$, and $\text{MAE} = 0.634\text{ m}^2\text{ m}^{-2}$. Moreover, the estimation errors are comparatively lower when we use the decomposition parameters. For $m - \chi$, the $\text{RMSE} = 0.736\text{ m}^2\text{ m}^{-2}$, and $\text{MAE} = 0.524\text{ m}^2\text{ m}^{-2}$. In comparison, the errors associated with estimates of PAI are lower using the $iS - \Omega$ scattering powers with CAL19-2/VAL19-2. We observe a higher dispersion of PAI estimates with RH-RV throughout the entire range of PAI. Besides, this estimation error with PAI might have likely propagated from the calibration phase of the WCM.

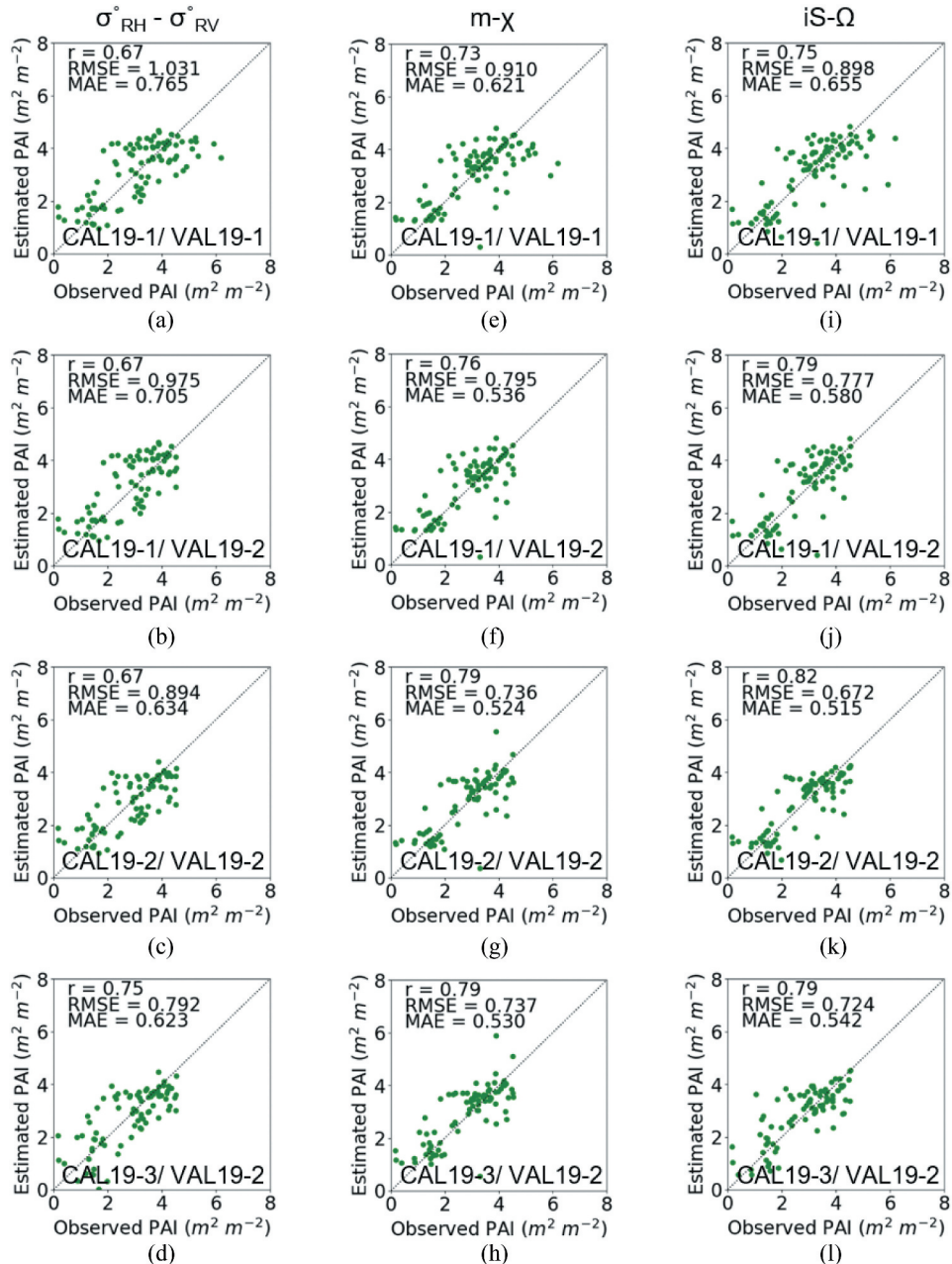


Figure 4. Cross-validation of PAI estimates with different calibration and validation data subsets pooled from observations of 2019. Scatter plots between observed and estimated PAI are grouped based on associated model (a-d) WCM $\sigma^{\circ}_{\text{RH}}$ and $\sigma^{\circ}_{\text{RV}}$, (e-h) MWCM $m - \chi$, and (i-l) MWCM $iS - \Omega$.

Considering the effect of rainfall in the calibration model for validation accuracy, the differences between CAL19-2/VAL19-2 and CAL19-3/VAL19-2 are not significant for these data sets. The error and correlation coefficients are similar, considering data sets from 2019. However, we can observe different validation results while transferring CAL19-2 and CAL19-3 to the 2018 validation cases for multi-year analysis (Sec. 4.3).

We note some interesting observations while restricting our analysis of PAI estimates from different growth stages and different PAI ranges. At the early stage of tillering with $\text{PAI} < 1.0 \text{ m}^2 \text{ m}^{-2}$, we observe an overestimation of PAI values for all the three models (RH-RV, $m - \chi$, and $iS - \Omega$). This condition is likely due to the backscatter response that is dominated by the underlying soil condition and standing water (Ulaby et al. 1984). As the plants grow, the PAI estimates closely follow the 1:1 line with the $iS - \Omega$ powers. This state is apparent during the advanced stages when rice plants are at tillering to booting stages. An improvement in PAI estimates during the heading to dough stage is noticeable for $iS - \Omega$ compared to the other two models.

Notably, we observe a higher variance in the case of RH-RV. The backscatter intensities are more sensitive to crop geometry and rice heads than changes in PAI or vegetation water content during these stages of rice development. However, when a scattering power decomposition is applied, it can better characterize the scattering phenomena than the direct use of backscatter intensities. In a separate experiment with full-pol SAR observations, Yang et al. (2016b) reported that the relative errors in LAI estimation from WCM and MWCM models are high ($\approx 6\text{-}10\%$) for rice. Also, during rice vegetative growth, the MWCM showed improved estimation accuracy of LAI with full-pol scattering power decompositions.

4.2. Analysis of 2018 data set

4.2.1. Model sensitivity analysis

Similar to the 2019 calibration results, the calibration accuracies for the 2018 data follow a similar response to the calibration data sets generated based on specific criteria, as presented in Table 3.

Considering a full range of PAI in the calibration data set (CAL18-1), the correlation coefficients (r) between the observed and simulated backscatter intensities are 0.65 (RH) and 0.61 (RV) for the calibration data, with a RMSE of $\approx 1.68\text{dB}$ and 1.78 dB . Improvements in accuracy are reported when scattering power decomposition elements are used in the MWCMs. For the $m - \chi$ decomposition, the correlation coefficients (r) between the observed and estimated scattering powers are 0.71 (P_v), 0.68 (P_s), and 0.64 (P_d). The RMSE is lowest for P_v (1.50 dB) as compared to P_s , and P_d (1.53 and 1.58, respectively). Similar to CAL19-1 results, the simulated $iS - \Omega$ decomposition parameters from the MWCM are better correlated with the observed scattering powers when compared to results from $m - \chi$ for CAL18-1. The RMSE is lowest (1.35 dB) for P_v as compared to P_s , and P_d (1.37 dB and 1.46 dB, respectively) for the $iS - \Omega$ decomposition parameters. It is also interesting to note that the error estimates decrease irrespective of vegetation models that are calibrated with datasets (CAL18-2) having a limited range of PAI between 0 and $4.5 \text{ m}^2 \cdot \text{m}^{-2}$ (Table 3). Amongst other models, $iS - \Omega$ scattering powers deliver the lowest RMSE values (1.21, 1.26, and 1.35 dB for P_v , P_s , and P_d , respectively) and high correlations with observed powers.

Unlike the 2019 data, there were no significant rainfall events during the acquisition dates of the SAR data in 2018. Hence, we have not analysed the impact of rainfall on the estimates for the 2018 data. Sensitivity plots are presented in [Figure 5](#) to assist in evaluating the results for several calibration models for 2018. Similar to 2019, these plots for 2018 display the simulated backscattered intensities and scattering powers as a function of PAI for saturated soil conditions. The values of incidence angles considered in each simulation in [Figure 5](#) are equal to the mean incidence angle of the RADARSAT-2 data acquired over the region.

Simulated results from CAL18-1 and CAL18-2 models indicate differential sensitivity of all components in the WCM and MWCM, arising mainly due to different ranges of PAI values during model calibrations. While considering a full range of PAI ($[0, 8]$) data sets (CAL18-1) during model calibration, the radar observables at higher PAI values ($> 4.5 \text{ m}^2 \text{ m}^{-2}$) are likely to be affected by saturation of the radar signal, which subsequently reduces sensitivity to changes in PAI. For the $\sigma_{\text{RH}}^{\circ}$ model in CAL18-1, the attenuated soil component contributes significantly to total backscatter with a range between -16 dB to -7.5 dB at $\text{PAI} < 4.5 \text{ m}^2 \text{ m}^{-2}$. This dynamic range of $\tau^2 \sigma_{\text{soil}}^{\circ}$ is comparatively higher than CAL19-1 of the 2019 data set. However, the vegetation contribution is considerably lower within a range of -40 dB to -15.5 dB . The $\sigma_{\text{RH}}^{\circ}$ is affected by the underlying soil surface to a greater extent than by the vegetation. However, for higher PAI values, the $\sigma_{\text{veg}}^{\circ}$ contribution is larger than $\tau^2 \sigma_{\text{soil}}^{\circ}$. The $\tau^2 \sigma_{\text{soil}}^{\circ}$ contribution decreased with a nonlinear rate. On the contrary, the variation in $\tau^2 \sigma_{\text{soil}}^{\circ}$ varied almost linearly in the CAL18-2 model of $\sigma_{\text{RH}}^{\circ}$.

We observe a differential sensitivity of $\sigma_{\text{total}}^{\circ}$ in $\sigma_{\text{RH}}^{\circ}$, when we calibrate the WCM with the CAL18-1 and CAL18-2 data sets. As compared to $\sigma_{\text{RH}}^{\circ}$, differential sensitivity between CAL18-1 and CAL18-2 is less pronounced in the case of $\sigma_{\text{RV}}^{\circ}$. We observe the saturation of $\sigma_{\text{total}}^{\circ}$ in RV at higher PAI values, which is likely due to attenuation of C-band signal within rice canopy. Considering the MWCM model elements in $m - \chi$ and $iS - \Omega$, we observe differences in power values with changes in PAI for CAL18-1 and CAL18-2 models. Similar to the 2019 data sets, at low PAI values ($< 1.5 \text{ m}^2 \text{ m}^{-2}$), the dominance of odd-bounce (P_s) scattering is apparent from both the decomposition techniques ($m - \chi$ and $iS - \Omega$) irrespective of CAL18-1 and CAL18-2 data sets. When we compared the decomposition methods, a 4% decrease in the P_s power is seen for the $iS - \Omega$ compared to the $m - \chi$ decomposition. In contrast, the diffuse scattering power is reduced by $\approx 10\%$ for the $iS - \Omega$ decompositions.

4.2.2. Validation of PAI estimates

We have analysed cross-validation performance with the calibration models and validation data sets from 2018 for retrieval of PAI. Each combination of CAL/VAL data is used for cross-validation, as shown in [Figure 6](#). We compared the estimated PAI with the in-situ measurements on a 1:1 plot to assess the retrieval performance of each model (WCM and MWCM) using the validation dataset.

The cross-validation experiment sets with 2018 data provide similar results to the 2019 data for PAI estimates, with RMSE varying from 0.743 to $1.123 \text{ m}^2 \text{ m}^{-2}$ and MAE varying from 0.579 to $0.867 \text{ m}^2 \text{ m}^{-2}$. Among these three CAL/VAL experiments, we observe the

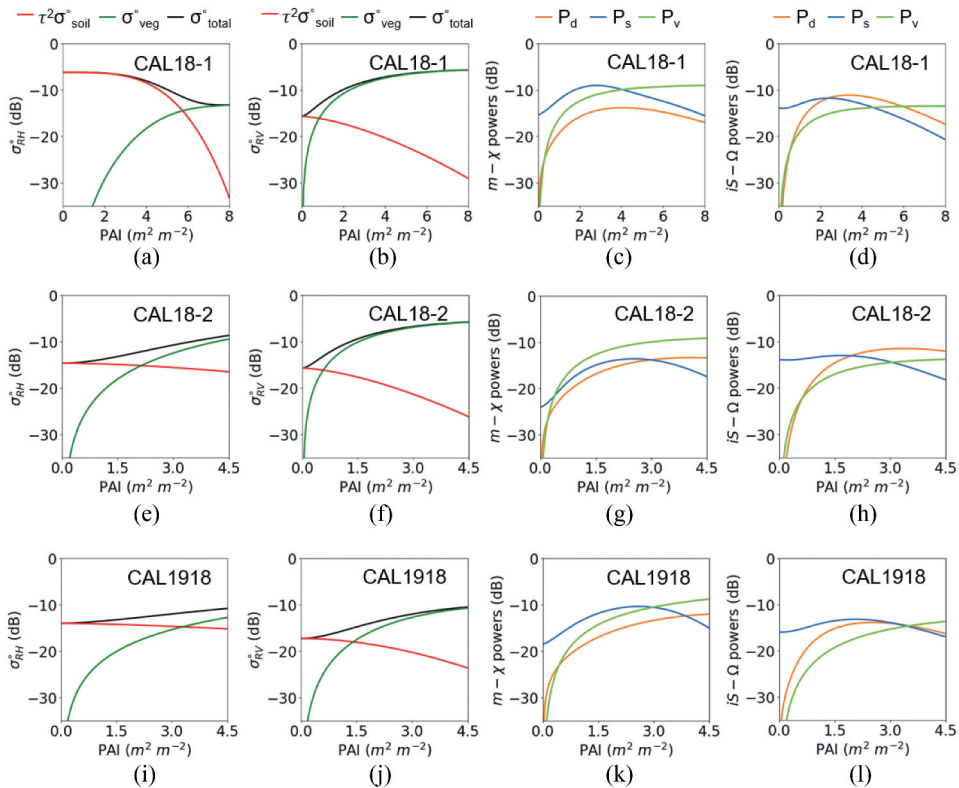


Figure 5. Simulations of backscatter powers with varying PAI ranges for WCM (σ_{RH}^o and σ_{RV}^o) and MWCMs ($m - \chi$ and $iS - \Omega$ decomposition powers) parameterized with different calibration data subsets pooled from observations of 2018. For CAL1918 models, data sets are pooled from both the 2019 and 2018 to include a largest ranges of backscatter powers values in calibration. Simulated parameters for (a-d) CAL18-1, (e-h) CAL18-2, and (i-l) CAL1918 data subsets.

highest error rates while utilizing the full range of PAI that was used for calibration and validation (CAL19-1/VAL19-1) for the three estimation options: $\sigma_{RH}^o - \sigma_{RV}^o$, $m - \chi$, and $iS - \Omega$.

The correlations between observed and estimated PAI values are highest ($r = 0.90$) for $iS - \Omega$ based retrievals, with RMSE and MAE of $0.763 \text{ m}^2 \text{ m}^{-2}$ and $0.590 \text{ m}^2 \text{ m}^{-2}$, respectively. While comparing calibration models, we found that the errors of estimation were relatively low when we used a restricted range of PAI in both the calibration and validation (CAL18-2/VAL18-2). For this particular combination, we observe the $\text{RMSE} = 0.743 \text{ m}^2 \text{ m}^{-2}$, and $\text{MAE} = 0.579 \text{ m}^2 \text{ m}^{-2}$ for the $iS - \Omega$ decomposition. Contrary to the 2019 analysis, variations in error rates for 2018 are less pronounced while switching calibration models in the CAL/VAL experiment.

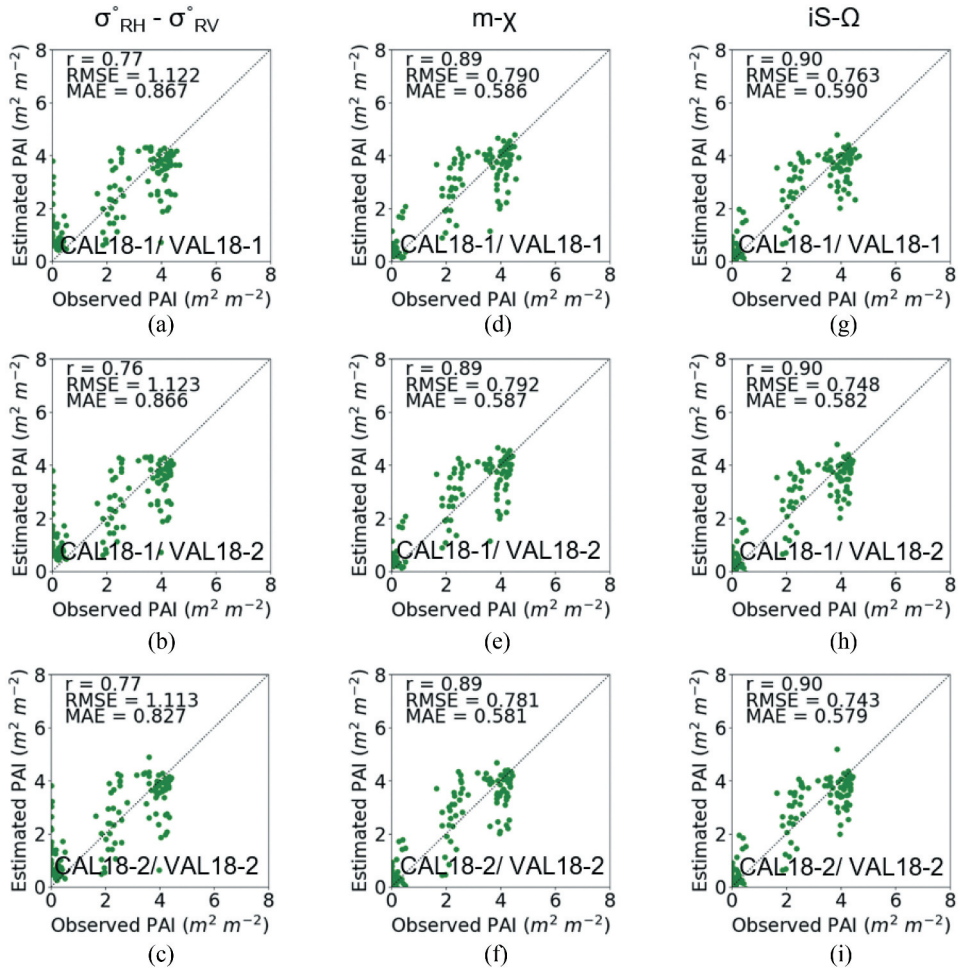


Figure 6. Cross-validation of PAI estimates with different calibration and validation data subsets pooled from observations of 2018. Scatter plots between observed and estimated PAI are grouped based on associated model (a-c) WCM σ°_{RH} and σ°_{RV} , (d-f) MWCM $m - \chi$, and (g-i) MWCM $iS - \Omega$.

4.3. Multi-year cross-validation

We analyse the temporal robustness of model calibration and validation by considering different criteria by selecting calibration data sets for each case and validating PAI retrieval for all other cases. Calibration model sensitivity plots are shown in Figures 3 and 5. We observe similar performances from the sensitivity plots for both 2018 and 2019 data, even though they have different distributions of values in the calibration data sets. To accommodate a broad range of backscatter power values in calibration, we combined CAL19-3 and CAL18-2 data sets from 2019 and 2018, respectively, to create a new data set, CAL1918.

The calibration results show that a broad range of SAR observables in the calibration data set enables good correlation and error estimates, as shown in Table 3. Individual results from 2019 and 2018 data sets show that the simulated $iS - \Omega$ decomposition

parameters from the MWCM are better correlated with the observed scattering powers when compared to results from $m - \chi$ for CAL1918. The RMSE values are lowest (1.22 dB, 1.31 dB, and 1.36 dB) for P_v , P_s , and P_d of the $iS - \Omega$ decomposition. The CAL1918 model sensitivity plots are also indicative of similar performances of SAR observables with changes in PAI values (Figure 5). In the multi-year CAL/VAL analysis, unlike single-year calibration/validation, we apply a calibration model developed for a single year and evaluated its performance in estimating PAI for the alternate year. The validation plots are shown in Figure 7. We report the highest accuracy for the $iS - \Omega$ based inversion while applying the 2018 calibration model to 2019 and validating the PAI estimates with 2019 in-situ data (CAL18-2/VAL19-2). The correlation coefficient, r between observed and estimated PAI is 0.76 with the lowest error (RMSE = $0.950 \text{ m}^2 \text{ m}^{-2}$ and MAE = $0.769 \text{ m}^2 \text{ m}^{-2}$). These results are similar to the validation error estimates using both CAL and VAL data from 2018 (Figure 6).

The $iS - \Omega$ based inversion shows the highest accuracy while applying the 2019 calibration model to 2018 and validating it with 2018 PAI measurements (CAL19-2/VAL18-2). The correlation coefficient, r between observed and estimated PAI is 0.86 with lower error (RMSE = $0.951 \text{ m}^2 \text{ m}^{-2}$ and MAE = $0.804 \text{ m}^2 \text{ m}^{-2}$) relative to RH-RV and $m - \chi$ based inversion. These results are similar to the validation error estimates using both CAL and VAL data from 2019 data sets (Figure 4).

It is also interesting to note that the validation results improved when selecting 2019 calibration data sets with no rainfall events (CAL19-3). The CAL19-3/VAL18-2 experiment indicated the highest accuracies for RH-RV, $m - \chi$, and $iS - \Omega$ based inversion approaches. Hence, caution should be taken while transferring calibration models from 1 year to another, especially if one data set is affected by rainfall or other precipitation events. Conventionally, we calibrate and validate the WCM using same year data. However, this study demonstrates the capability of transferring a model calibrated from 1 year to another with consistent performance.

In another set of experiments, we combined data from multiple years to create a calibration data set. In this case, we observe a comparatively lower error in PAI estimates relative to the use of a model calibrated with a single year of data (Figure 8). Here, we use the CAL1918 data to calibrate the WCM and MWCM, then validate PAI estimates with a single year (VAL18-2 and VAL19-2) and multi-year data (VAL1918). For the CAL1918/VAL18-2 experiment, we observed the highest correlation ($r=0.93$) between observed and estimated PAI with lowest errors values (RMSE = $0.645 \text{ m}^2 \text{ m}^{-2}$ and MAE = $0.482 \text{ m}^2 \text{ m}^{-2}$) using inversion from $iS - \Omega$.

In contrast, the RH-RV and $m - \chi$ based inversions provided RMSE and MAE $> 0.90 \text{ m}^2 \text{ m}^{-2}$ and $> 0.740 \text{ m}^2 \text{ m}^{-2}$ respectively. We also observe the efficacy of $iS - \Omega$ based inversion for CAL6/VAL19-2 experiments. However, the error rates are marginally better in these experiments. These experiments indicate that cross-validation performance improves using a sizable number of observations to calibrate the model (either WCM or MWCMs). It makes the model more suited for independent data sets. Such an approach provides a wider range of realizations in the calibration data set (i.e. a combination of multiple-year data sets).

The multi-year validation data also provided reasonable accuracy, as shown by CAL1918/VAL1918 results (Figure 8). When comparing the inversion approaches, the validation error exhibits improvements using the $iS - \Omega$ based method. This scenario

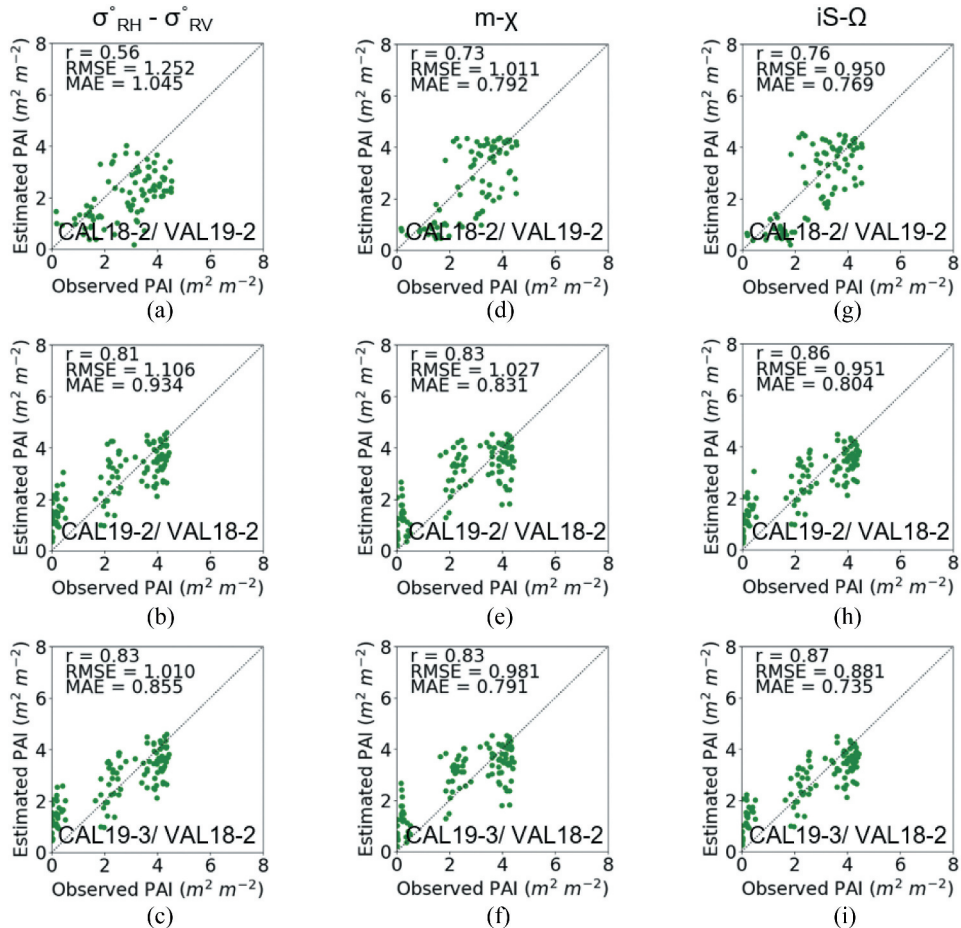


Figure 7. Cross-validation of PAI estimates with different calibration and validation data subsets pooled from observations of 2019 and 2018. In this strategy, the calibration model developed for a year and then transferred it to another year followed by validating PAI estimate with the another year data. Scatter plots between observed and estimated PAI are grouped based on associated model (a-c) WCM σ°_{RH} and σ°_{RV} , (d-f) MWCM $m - \chi$, and (g-i) MWCM $iS - \Omega$.

delivers the highest correlation ($r=0.90$) along with the lowest RMSE and MAE error of $0.666\text{ m}^2\text{ m}^{-2}$ and $0.486\text{ m}^2\text{ m}^{-2}$, respectively. We also observe a higher dispersion of PAI estimates with RH-RV throughout the entire range of PAI. This estimation error with PAI may have propagated from the calibration phase of the WCM.

5. Conclusion

In this multi-year experiment, we compared the retrieval of the Plant Area Index (PAI) using three options:

- σ°_{RH} and σ°_{RV} based Water Cloud Model (WCM) inversion
- $m - \chi$ scattering powers based Modified WCM (MWCM)
- $iS - \Omega$ scattering powers based MWCM

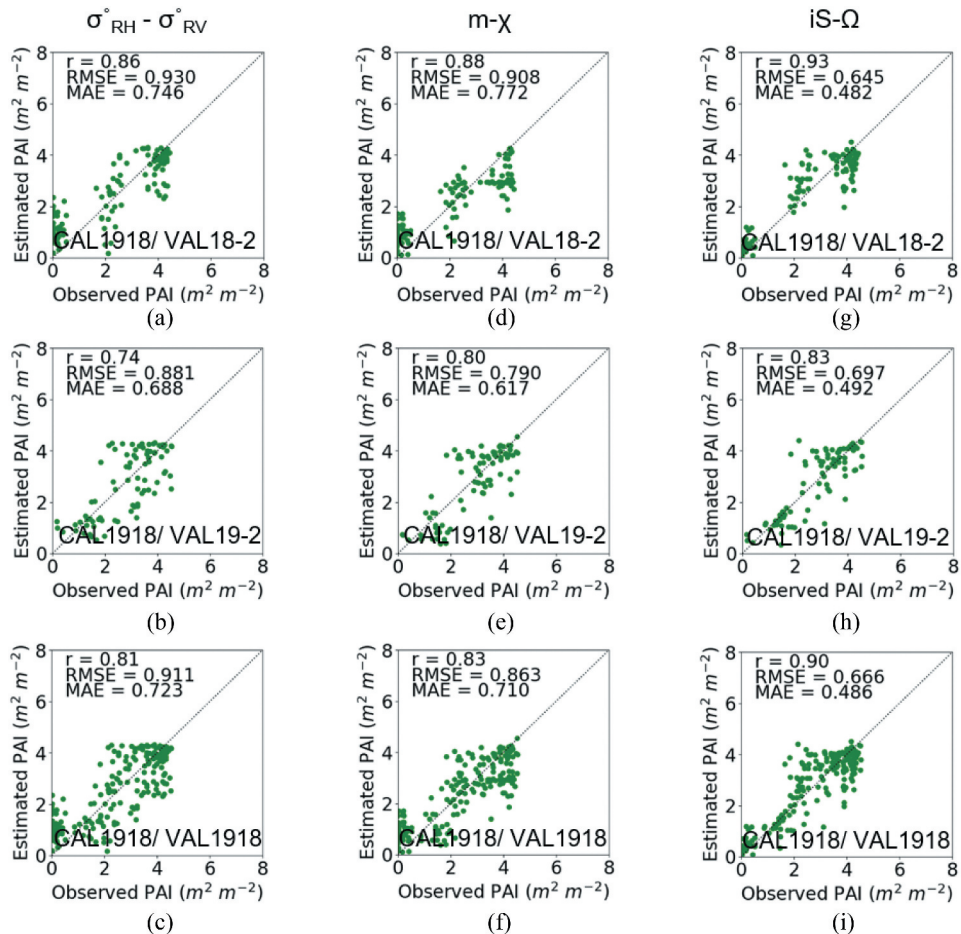


Figure 8. Cross-validation of PAI estimates with different calibration and validation data subsets pooled from observations of 2019 and 2018. In this strategy, we combined data from multiple years in calibration data sets. Scatter plots between observed and estimated PAI are grouped based on associated model (a-c) WCM σ_{RH}° and σ_{RV}° , (d-f) MWCM $m - \chi$, and (g-i) MWCM $iS - \Omega$.

Model calibration and validation (both in single and multi-year analysis) provided high correlation coefficients and low estimation errors for MWCM simulations and PAI estimates. The use of scattering power components, i.e.: odd-bounce (P_s), even-bounce (P_d), and diffuse power (P_v) from the compact-pol SAR (CP SAR) power decomposition ($m - \chi$ or $iS - \Omega$) improves the PAI estimates from the MWCM when compared with estimates from RH-RV backscatter intensities and the WCM. The validation accuracy indicates a lower correlation between the observed and estimated PAI and higher error for σ_{RH}° - σ_{RV}° based WCM inversion approach.

We achieved a significant improvement in PAI retrieval in terms of lower retrieval errors using the proposed $iS - \Omega$ decomposition compared to other decomposition methods (i.e. Root Mean Square Error (RMSE) of approximately $0.586 \text{ m}^2 \text{ m}^{-2}$, and Mean Absolute Error (MAE) of $0.443 \text{ m}^2 \text{ m}^{-2}$). Hence, to estimate crop biophysical parameters such as PAI,

this study recommends using scattering power from the $iS - \Omega$ decomposition and the MWCM for biophysical parameter retrieval for compact-pol Circular Transmit-Linear Receive (CTLR) observations.

The multi-year cross-validation results suggest that the utility of calibration data transfer from one experimental data set to another, even when acquired in different years, is possible. The $iS - \Omega$ based inversion produced the highest accuracy when the 2019 calibration model was applied to estimate PAI with 2018 data (CAL19-2/VAL18-2). The r between observed and estimated PAI is 0.86 with low errors (RMSE = 0.951 and MAE = 0.804). Thus confirming the better performance of the $iS - \Omega$ scattering powers relative to approaches using the RH-RV and $m - \chi$ based inversions. These results are similar to the validation errors using both calibration and validation data from a single year. Validation results improved when we selected calibration data sets where we excluded rainfall events. While in most cases, the WCM and MWCMs are calibrated and validated on the data subsets of single seasons. In this regard, our results confirm the capability of transferring a model calibrated from 1 year to another with consistent performance.

The proposed inversion of the MWCM with the scattering powers derived from CP SAR data will be of significant interest from an operational perspective for the RADARSAT Constellation Mission (RCM) and upcoming CP enabled missions RISAT-1A and NISAR. In particular, the RCM is capable of acquiring CP data at swaths of up to 500 km with different noise equivalent sigma zero (NESZ) values. Given these promising results, implementing compact-pol data from these missions, in terms of transmitted circularity and NESZ, requires further exploration. In this current study, the analysis is limited to a single test site, and as such, local adjustments of the model might be required for other sites. Hence, the robustness of these inversion strategies should be tested over other agricultural regions and cropping systems within a cross-site experiment framework.

Acknowledgements

The authors would like to thank the Canadian Space Agency and MAXAR Technologies Ltd. (formerly MDA) for providing the RADARSAT-2 images through the Joint Experiment for Crop Assessment and Monitoring (JECAM) SAR Inter-comparison experiment network. The authors are also thankful to the Andhra Pradesh Space Application Centre (APSAC), ITE & C Department, Government of Andhra Pradesh for support during the field campaigns. The authors acknowledge the GEO-AWS Earth Observation Cloud Credits Program, which supported the computation on AWS cloud platform through the project "AWS4AgriSAR-Crop inventory mapping from SAR data on cloud computing platform." This work was supported in part by the Shastri Indo Canadian Institute, New Delhi, India, through the Shastri Research Student Fellowship (2018–2019) grant for the project "Estimation of crop biophysical parameters using Polarimetric Synthetic Aperture Radar (SAR) Remote Sensing Data."

Disclosure statement

No potential conflict of interest was reported by the author(s).



Funding

This work was supported by the Shastri Indo-Canadian Institute.

ORCID

Dipankar Mandal <http://orcid.org/0000-0001-8407-7125>
 Vineet Kumar <http://orcid.org/0000-0002-0469-3815>
 Avik Bhattacharya <http://orcid.org/0000-0001-6720-6108>
 Heather McNairn <http://orcid.org/0000-0003-1006-0018>

Codes

We made available the code that supports the reproducibility and replicability of this work in a Github repository: <https://github.com/dipankar05/IJRS-MWCM>.

Data availability statement (DAS)

Due to the nature of this research, participants of this study did not agree for their data to be shared publicly, so supporting data is not available.

References

- Aiello, A., and J. P. Woerdman. 2005. "Physical Bounds to the Entropy-depolarization Relation in Random Light Scattering." *Physical Review Letters* 94 (9): 090406. doi:[10.1103/PhysRevLett.94.090406](https://doi.org/10.1103/PhysRevLett.94.090406).
- Ainsworth, T. L., J. P. Kelly, and J.-S. Lee. 2009. "Classification Comparisons between Dual-pol, Compact Polarimetric and Quad-pol SAR Imagery." *ISPRS Journal of Photogrammetry and Remote Sensing* 64 (5): 464–471. doi:[10.1016/j.isprsjprs.2008.12.008](https://doi.org/10.1016/j.isprsjprs.2008.12.008).
- Attema, E. P. W., and F. T. Ulaby. 1978. "Vegetation Modeled as a Water Cloud." *Radio Science* 13 (2): 357–364. doi:[10.1029/RS013i002p00357](https://doi.org/10.1029/RS013i002p00357).
- Ballester-Berman, J. D., and J. M. Lopez-Sanchez. 2012. "Time Series of Hybrid-polarity Parameters over Agricultural Crops." *IEEE Geoscience and Remote Sensing Letters* 9 (1): 139–143. doi:[10.1109/LGRS.2011.2162312](https://doi.org/10.1109/LGRS.2011.2162312).
- Beriaux, E., C. Lucau-Danila, E. Auquiere, and P. Defourny. 2013. "Multiyear Independent Validation of the Water Cloud Model for Retrieving Maize Leaf Area Index from SAR Time Series." *International Journal of Remote Sensing* 34 (12): 4156–4181. doi:[10.1080/01431161.2013.772676](https://doi.org/10.1080/01431161.2013.772676).
- Bériaux, E., F. Waldner, F. Collienne, P. Bogaert, and P. Defourny. 2015. "Maize Leaf Area Index Retrieval from Synthetic Quad Pol SAR Time Series Using the Water Cloud Model." *Remote Sensing* 7 (12): 16204–16225. doi:[10.3390/rs71215818](https://doi.org/10.3390/rs71215818).
- Bhattacharya, A., S. De, A. Muhuri, M. Surendar, G. Venkataraman, and A. K. Das. 2015. "A New Compact Polarimetric SAR Decomposition Technique." *Remote Sensing Letters* 6 (12): 914–923. doi:[10.1080/2150704X.2015.1088669](https://doi.org/10.1080/2150704X.2015.1088669).
- Breda, N. J. J. 2003. "Ground-based Measurements of Leaf Area Index: A Review of Methods, Instruments and Current Controversies." *Journal of Experimental Botany* 54 (392): 2403–2417. doi:[10.1093/jxb/erg263](https://doi.org/10.1093/jxb/erg263).
- Brisco, B., L. Kun, B. Tedford, F. Charbonneau, S. Yun, and K. Murnaghan. 2013. "Compact Polarimetry Assessment for Rice and Wetland Mapping." *International Journal of Remote Sensing* 34 (6): 1949–1964. doi:[10.1080/01431161.2012.730156](https://doi.org/10.1080/01431161.2012.730156).

- Charbonneau, F. J., B. Brisco, R. K. Raney, H. McNairn, C. Liu, P. W. Vachon, J. Shang, et al. 2010. "Compact Polarimetry Overview and Applications Assessment." *Canadian Journal of Remote Sensing* 36 (sup2): S298–S315. DOI:[10.5589/m10-062](https://doi.org/10.5589/m10-062).
- Chauhan, S., H. S. Srivastava, and P. Patel. 2017. "Improved Parameterization of Water Cloud Model for Hybrid-polarized Backscatter Simulation Using Interaction Factor." *International Archives of the Photogrammetry, Remote Sensing & Spatial Information Sciences* 42.
- Chauhan, S., H. S. Srivastava, and P. Patel. 2018. "Wheat Crop Biophysical Parameters Retrieval Using Hybrid-polarized RISAT-1 SAR Data." *Remote Sensing of Environment* 216: 28–43. doi:[10.1016/j.rse.2018.06.014](https://doi.org/10.1016/j.rse.2018.06.014).
- Cloude, S. R., D. G. Goodenough, and H. Chen. 2012. "Compact Decomposition Theory." *IEEE Geoscience and Remote Sensing Letters* 9 (1): 28–32. doi:[10.1109/LGRS.2011.2158983](https://doi.org/10.1109/LGRS.2011.2158983).
- Dabrowska-Zielinska, K., Y. Inoue, W. Kowalik, and M. Gruszczynska. 2007. "Inferring the Effect of Plant and Soil Variables on C-and L-band SAR Backscatter over Agricultural Fields, Based on Model Analysis." *Advances in Space Research* 39 (1): 139–148. doi:[10.1016/j.asr.2006.02.032](https://doi.org/10.1016/j.asr.2006.02.032).
- Dave, V. A., D. Haldar, R. Dave, A. Misra, and V. Pandey. 2017. "Cotton Crop Biophysical Parameter Study Using Hybrid/compact Polarimetric RISAT-1 SAR Data." *Progress In Electromagnetics Research* 57: 185–196. doi:[10.2528/PIERM16121903](https://doi.org/10.2528/PIERM16121903).
- Davidson, A., H. McNairn, M. Hosseini, and L. Dingle-Robertson. 2017. "JECAM Synthetic Aperture Radar (SAR) Inter-Comparison Experiment." <http://jecam.org/experiment/sar-intercomparison/>
- De Roo, R. D., Y. Du, F. T. Ulaby, and M. Craig Dobson. 2001. "A Semi-empirical Backscattering Model at L-band and C-band for A Soybean Canopy with Soil Moisture Inversion." *IEEE Transactions on Geoscience and Remote Sensing* 39 (4): 864–872. doi:[10.1109/36.917912](https://doi.org/10.1109/36.917912).
- Dey, S., A. Bhattacharya, D. Ratha, D. Mandal, H. McNairn, J. M. Lopez-Sanchez, and Y. S. Rao. 2020. "Novel Clustering Schemes for Full and Compact Polarimetric SAR Data: An Application for Rice Phenology Characterization." *ISPRS Journal of Photogrammetry and Remote Sensing* 169: 135–151. doi:[10.1016/j.isprsjprs.2020.09.010](https://doi.org/10.1016/j.isprsjprs.2020.09.010).
- Dingle Robertson, L., M. Hosseini, A. M. Davidson, and H. McNairn. 2017. "The Joint Experiment for Crop Assessment and Monitoring (JECAM): Synthetic Aperture Radar (SAR) Inter-Comparison Experiment." In *Agufm 2017*, American Geophysical Union, Fall Meeting abstract. B51C-1804.
- ESA. 2019. "Science Toolbox Exploration Platform." <https://step.esa.int/main/snap-7-0-released/>
- Graham, A. J., and R. Harris. 2003. "Extracting Biophysical Parameters from Remotely Sensed Radar Data: A Review of the Water Cloud Model." *Progress in Physical Geography* 27 (2): 217–229. doi:[10.1191/030913303pp378ra](https://doi.org/10.1191/030913303pp378ra).
- Guo, X., K. Li, Y. Shao, Z. Wang, H. Li, Z. Yang, L. Liu, and S. Wang. 2018. "Inversion of Rice Biophysical Parameters Using Simulated Compact Polarimetric SAR C-band Data." *Sensors* 18 (7): 2271. doi:[10.3390/s18072271](https://doi.org/10.3390/s18072271).
- Hajj, E., N. B. Mohammad, and M. Zribi. 2019. "Comparative Analysis of the Accuracy of Surface Soil Moisture Estimation from the C-and L-bands." *International Journal of Applied Earth Observation and Geoinformation* 82: 101888. doi:[10.1016/j.jag.2019.05.021](https://doi.org/10.1016/j.jag.2019.05.021).
- Homayouni, S., H. McNairn, M. Hosseini, X. Jiao, and J. Powers. 2019. "Quad and Compact Multitemporal C-band PolSAR Observations for Crop Characterization and Monitoring." *International Journal of Applied Earth Observation and Geoinformation* 74: 78–87. doi:[10.1016/j.jag.2018.09.009](https://doi.org/10.1016/j.jag.2018.09.009).
- Hosseini, M., and H. McNairn. 2017. "Using Multi-polarization C-and L-band Synthetic Aperture Radar to Estimate Biomass and Soil Moisture of Wheat Fields." *International Journal of Applied Earth Observation and Geoinformation* 58: 50–64. doi:[10.1016/j.jag.2017.01.006](https://doi.org/10.1016/j.jag.2017.01.006).
- Hosseini, M., H. McNairn, A. Merzouki, and A. Pacheco. 2015. "Estimation of Leaf Area Index (LAI) in Corn and Soybeans Using Multi-polarization C-and L-band Radar Data." *Remote Sensing of Environment* 170: 77–89. doi:[10.1016/j.rse.2015.09.002](https://doi.org/10.1016/j.rse.2015.09.002).
- Hosseini, M., H. McNairn, S. Mitchell, L. D. Robertson, A. Davidson, N. Ahmadian, A. Bhattacharya, et al. 2021. "A Comparison between Support Vector Machine and Water Cloud Model for Estimating Crop Leaf Area Index." *Remote Sensing* 13 (7): 1348. DOI:[10.3390/rs13071348](https://doi.org/10.3390/rs13071348).



- Inoue, Y., T. Kurosu, H. Maeno, S. Uratsuka, T. Kozu, K. Dabrowska-Zielinska, and J. Qi. 2002. "Season-long Daily Measurements of Multifrequency (Ka, Ku, X, C, and L) and Full-polarization Backscatter Signatures over Paddy Rice Field and Their Relationship with Biological Variables." *Remote Sensing of Environment* 81 (2–3): 194–204. doi:10.1016/S0034-4257(01)00343-1.
- INRA. 2017. "CAN-EYE." <https://www6.paca.inra.fr/can-eye>
- Jonckheere, I., S. Fleck, K. Nackaerts, B. Muys, P. Coppin, M. Weiss, and F. Baret. 2004. "Review of Methods for in Situ Leaf Area Index Determination: Part I. Theories, Sensors and Hemispherical Photography." *Agricultural and Forest Meteorology* 121 (1–2): 19–35. doi:10.1016/j.agrformet.2003.08.027.
- Keith, R. R., T. S. Joshua, C. G. Wesley Patterson, D. Benjamin, and J. Bussey. 2012. "The M-chi Decomposition of Hybrid Dual-polarimetric Radar Data with Application to Lunar Craters." *Journal of Geophysical Research: Planets* 117 (E12): n/a–n/a. doi:10.1029/2011JE003986.
- Kumar, V., D. Mandal, A. Bhattacharya, and Y. S. Rao. 2020. "Crop Characterization Using an Improved Scattering Power Decomposition Technique for Compact Polarimetric SAR Data." *International Journal of Applied Earth Observation and Geoinformation* 88: 102052. doi:10.1016/j.jag.2020.102052.
- Kumar, V., H. McNairn, A. Bhattacharya, and Y. S. Rao. 2017. "Temporal Response of Scattering from Crops for Transmitted Ellipticity Variation in Simulated Compact-Pol SAR Data." *IEEE Journal of Selected Topics in Applied Earth Observations and Remote Sensing* 10 (12): 5163–5174.
- Kumar, V., Y. S. Rao, A. Bhattacharya, and S. R. Cloude. 2019. "Classification Assessment of Real versus Simulated Compact and Quad-Pol Modes of ALOS-2." *IEEE Geoscience and Remote Sensing Letters* 16: 1497–1501. doi:10.1109/LGRS.2019.2899268.
- Kweon, S.-K., and O. Yisok. 2015. "A Modified Water-cloud Model with Leaf Angle Parameters for Microwave Backscattering from Agricultural Fields." *IEEE Transactions on Geoscience and Remote Sensing* 53 (5): 2802–2809. doi:10.1109/TGRS.2014.2364914.
- Le Toan, T., F. Ribbes, L.-F. Wang, N. Flouri, K.-H. Ding, J. A. Kong, M. Fujita, and T. Kurosu. 1997. "Rice Crop Mapping and Monitoring Using ERS-1 Data Based on Experiment and Modeling Results." *IEEE Transactions on Geoscience and Remote Sensing* 35 (1): 41–56. doi:10.1109/36.551933.
- Lievens, H., and N. E. C. Verhoest. 2011. "On the Retrieval of Soil Moisture in Wheat Fields from L-band SAR Based on Water Cloud Modeling, the IEM, and Effective Roughness Parameters." *IEEE Geoscience and Remote Sensing Letters* 8 (4): 740–744. doi:10.1109/LGRS.2011.2106109.
- Lopez-Sanchez, J. M., F. Vicente-Guijalba, J. David Ballester-Berman, and S. R. Cloude. 2014. "Polarimetric Response of Rice Fields at C-band: Analysis and Phenology Retrieval." *IEEE Transactions on Geoscience and Remote Sensing* 52 (5): 2977–2993. doi:10.1109/TGRS.2013.2268319.
- Mahdianpari, M., F. Mohammadimanesh, H. McNairn, A. Davidson, M. Rezaee, B. Salehi, and S. Homayouni. 2019. "Mid-season Crop Classification Using Dual-, Compact-, and Full-Polarization in Preparation for the Radarsat Constellation Mission (RCM)." *Remote Sensing* 11 (13): 1582. doi:10.3390/rs11131582.
- Mandal, D., A. Bhattacharya, and Y. S. Rao. 2021. *Radar Remote Sensing for Crop Biophysical Parameter Estimation*. Singapore: Springer.
- Mandal, D., D. Ratha, A. Bhattacharya, V. Kumar, H. McNairn, Y. S. Rao, and A. C. Frery. 2020. "A Radar Vegetation Index for Crop Monitoring Using Compact Polarimetric SAR Data." *IEEE Transactions on Geoscience and Remote Sensing* 58: 6321–6335. doi:10.1109/TGRS.2020.2976661.
- Mandal, D., M. Hosseini, H. McNairn, V. Kumar, A. Bhattacharya, Y. S. Rao, S. Mitchell, L. D. Robertson, A. Davidson, and K. Dabrowska-Zielinska. 2019b. "An Investigation of Inversion Methodologies to Retrieve the Leaf Area Index of Corn from C-band SAR Data." *International Journal of Applied Earth Observation and Geoinformation* 82: 101893. doi:10.1016/j.jag.2019.06.003.
- Mandal, D., V. Kumar, A. Bhattacharya, and Y. S. Rao. 2017. "JECAM Site in India-Vijayawada." <http://jecam.org/studysite/India-vijayawada/>
- Mandal, D., V. Kumar, H. McNairn, A. Bhattacharya, and Y. S. Rao. 2019c. "Joint Estimation of Plant Area Index (PAI) and Wet Biomass in Wheat and Soybean from C-band Polarimetric SAR Data." *International Journal of Applied Earth Observation and Geoinformation* 79: 24–34. doi:10.1016/j.jag.2019.02.007.

- Mandal, D., V. Kumar, Y. S. Rao, A. Bhattacharya, and K. V. Ramana. 2019a. "Experimental Field Campaigns at Vijayawada Test Site." Technical Report MRS2019TR02. Microwave Remote Sensing Lab, India. doi:[10.17605/OSF.IO/DN3E8](https://doi.org/10.17605/OSF.IO/DN3E8).
- McNairn, H., S. Homayouni, M. Hosseini, J. Powers, K. Beckett, and W. Parkinson. 2017. "Compact Polarimetric Synthetic Aperture Radar for Monitoring Crop Condition." In *Proc. IEEE Int. Geosci. Remote Sens. Symp.*, 4358–4361. Texas, USA: IEEE.
- Merzouki, A., H. McNairn, J. Powers, and M. Friesen. 2019. "Synthetic Aperture Radar (SAR) Compact Polarimetry for Soil Moisture Retrieval." *Remote Sensing* 11 (19): 2227. doi:[10.3390/rs11192227](https://doi.org/10.3390/rs11192227).
- Misra, T., S. S. Rana, N. M. Desai, D. B. Dave, R. K. A. Rajeevjiyoti, C. V. N. Rao, B. V. Bakori, R. Neelakantan, and J. G. Vachhani. 2013. "Synthetic Aperture Radar Payload On-board RISAT-1: Configuration, Technology and Performance." *Current Science* 104 (4): 446–461.
- Moré, J. J. 1978. "The Levenberg-Marquardt Algorithm: Implementation and Theory." In: Watson G.A. (eds) *Numerical Analysis. Lecture Notes in Mathematics*, vol 630. Springer, Berlin, Heidelberg.
- Neumann, H. H., G. Den Hartog, and R. H. Shaw. 1989. "Leaf Area Measurements Based on Hemispheric Photographs and Leaf-litter Collection in a Deciduous Forest during Autumn Leaf-fall." *Agricultural and Forest Meteorology* 45 (3–4): 325–345. doi:[10.1016/0168-1923\(89\)90052-X](https://doi.org/10.1016/0168-1923(89)90052-X).
- Nord, M. E., T. L. Ainsworth, J.-S. Lee, and N. J. S. Stacy. 2009. "Comparison of Compact Polarimetric Synthetic Aperture Radar Modes." *IEEE Transactions on Geoscience and Remote Sensing* 47 (1): 174–188. doi:[10.1109/TGRS.2008.2000925](https://doi.org/10.1109/TGRS.2008.2000925).
- Ohki, M., and M. Shimada. 2018. "Large-Area Land Use and Land Cover Classification with Quad, Compact, and Dual Polarization SAR Data by PALSAR-2." *IEEE Transactions on Geoscience and Remote Sensing* 56 (9): 5550–5557. doi:[10.1109/TGRS.2018.2819694](https://doi.org/10.1109/TGRS.2018.2819694).
- Ouellette, J. D., J. T. Johnson, S. Kim, J. J. van Zyl, M. Moghaddam, M. W. Spencer, L. Tsang, and D. Entekhabi. 2014. "A Simulation Study of Compact Polarimetry for Radar Retrieval of Soil Moisture." *IEEE Transactions on Geoscience and Remote Sensing* 52 (9): 5966–5973. doi:[10.1109/TGRS.2013.2294133](https://doi.org/10.1109/TGRS.2013.2294133).
- Ponnurangam, G. G., T. Jagdhuber, I. Hajnsek, and Y. S. Rao. 2016. "Soil Moisture Estimation Using Hybrid Polarimetric SAR Data of RISAT-1." *IEEE Transactions on Geoscience and Remote Sensing* 54 (4): 2033–2049. doi:[10.1109/TGRS.2015.2494860](https://doi.org/10.1109/TGRS.2015.2494860).
- Prevot, L., I. Champion, and G. Guyot. 1993. "Estimating Surface Soil Moisture and Leaf Area Index of a Wheat Canopy Using a Dual-frequency (C and X Bands) Scatterometer." *Remote Sensing of Environment* 46 (3): 331–339. doi:[10.1016/0034-4257\(93\)90053-Z](https://doi.org/10.1016/0034-4257(93)90053-Z).
- Raney, R. K., B. Brisco, M. Dabboor, and M. Mahdianpari. 2021. "RADARSAT Constellation Mission's Operational Polarimetric Modes: A User-Driven Radar Architecture." *Canadian Journal of Remote Sensing* 47: 1–16. doi:[10.1080/07038992.2021.1907566](https://doi.org/10.1080/07038992.2021.1907566).
- Raney, R. K. 2007. "Hybrid-polarity SAR Architecture." *IEEE Transactions on Geoscience and Remote Sensing* 45 (11): 3397–3404. doi:[10.1109/TGRS.2007.895883](https://doi.org/10.1109/TGRS.2007.895883).
- Raney, R. K. 2016. "Comparing Compact and Quadrature Polarimetric SAR Performance." *IEEE Geoscience and Remote Sensing Letters* 13 (6): 861–864. doi:[10.1109/LGRS.2016.2550863](https://doi.org/10.1109/LGRS.2016.2550863).
- Raney, R. K. 2019. "Hybrid Dual-Polarization Synthetic Aperture Radar." *Remote Sensing* 11 (13): 1521. doi:[10.3390/rs11131521](https://doi.org/10.3390/rs11131521).
- Shang, J., H. McNairn, F. Charbonneau, Z. Chen, and X. Jiao. 2012. "Sensitivity Analysis of Compact Polarimetry Parameters to Crop Growth Using Simulated RADARSAT-2 SAR Data." In *2012 IEEE International Geoscience and Remote Sensing Symposium*, 1825–1828. Munich, Germany: IEEE.
- Steele-Dunne, S. C., H. McNairn, A. Monsivais-Huertero, J. Judge, P. Liu, and K. Papathanassiou. 2017. "Radar Remote Sensing of Agricultural Canopies: A Review." *IEEE Journal of Selected Topics in Applied Earth Observations and Remote Sensing* 10 (5): 2249–2273. doi:[10.1109/JSTARS.2016.2639043](https://doi.org/10.1109/JSTARS.2016.2639043).
- Thompson, A. A. 2015. "Overview of the RADARSAT Constellation Mission." *Canadian Journal of Remote Sensing* 41 (5): 401–407. doi:[10.1080/07038992.2015.1104633](https://doi.org/10.1080/07038992.2015.1104633).
- Touzi, R., and F. Charbonneau. 2014. "Requirements on the Calibration of Hybrid-compact SAR." In *2014 IEEE Geoscience and Remote Sensing Symposium*, 1109–1112. Quebec, Canada: IEEE.

- Truong-Loi, M.-L., A. Freeman, P. C. Dubois-Fernandez, and E. Pottier. 2009. "Estimation of Soil Moisture and Faraday Rotation from Bare Surfaces Using Compact Polarimetry." *IEEE Transactions on Geoscience and Remote Sensing* 47 (11): 3608–3615. doi:[10.1109/TGRS.2009.2031428](https://doi.org/10.1109/TGRS.2009.2031428).
- Ulaby, F. T., C. T. Allen, G. Eger Iii, and E. Kanemasu. 1984. "Relating the Microwave Backscattering Coefficient to Leaf Area Index." *Remote Sensing of Environment* 14 (1–3): 113–133. doi:[10.1016/0034-4257\(84\)90010-5](https://doi.org/10.1016/0034-4257(84)90010-5).
- Ulaby, F., and D. Long. 2015. *Microwave Radar and Radiometric Remote Sensing*. Boston, USA: Artech House.
- Venkata, K., S. P. Ramana, S. S. Mullapudi Venkata Rama, A. Gogineni, D. Prabir Kumar, R. Allakki Venkata, A. Nagaraju, V. K. Dadhwali, and K. R. P. Singh. 2017. "Multi-incidence Angle RISAT-1 Hybrid Polarimetric SAR Data for Large Area Mapping of Maize Crop—a Case Study in Khagaria District, Bihar, India." *International Journal of Remote Sensing* 38 (20): 5487–5501. doi:[10.1080/01431161.2017.1338783](https://doi.org/10.1080/01431161.2017.1338783).
- Wang, C., J. Wu, Y. Zhang, G. Pan, J. Qi, and W. A. Salas. 2009. "Characterizing L-band Scattering of Paddy Rice in Southeast China with Radiative Transfer Model and Multitemporal ALOS/PALSAR Imagery." *IEEE Transactions on Geoscience and Remote Sensing* 47 (4): 988–998. doi:[10.1109/TGRS.2008.2008309](https://doi.org/10.1109/TGRS.2008.2008309).
- Weiss, M., F. Baret, G. J. Smith, I. Jonckheere, and P. Coppin. 2004. "Review of Methods for in Situ Leaf Area Index (LAI) Determination: Part II. Estimation of LAI, Errors and Sampling." *Agricultural and Forest Meteorology* 121 (1–2): 37–53. doi:[10.1016/j.agrformet.2003.08.001](https://doi.org/10.1016/j.agrformet.2003.08.001).
- Wigneron, J.-P., P. Ferrazzoli, A. Olioso, P. Bertuzzi, and A. Chanzy. 1999. "A Simple Approach to Monitor Crop Biomass from C-band Radar Data." *Remote Sensing of Environment* 69 (2): 179–188. doi:[10.1016/S0034-4257\(99\)00011-5](https://doi.org/10.1016/S0034-4257(99)00011-5).
- Xie, L., H. Zhang, F. Wu, C. Wang, and B. Zhang. 2015b. "Capability of Rice Mapping Using Hybrid Polarimetric SAR Data." *IEEE Journal of Selected Topics in Applied Earth Observations and Remote Sensing* 8 (8): 3812–3822. doi:[10.1109/JSTARS.2014.2387214](https://doi.org/10.1109/JSTARS.2014.2387214).
- Xie, L., H. Zhang, H. Li, and C. Wang. 2015. "A Unified Framework for Crop Classification in Southern China Using Fully Polarimetric, Dual Polarimetric, and Compact Polarimetric SAR Data." *International Journal of Remote Sensing* 36 (14): 3798–3818. doi:[10.1080/01431161.2015.1070319](https://doi.org/10.1080/01431161.2015.1070319).
- Xing, M., B. He, X. Ni, J. Wang, G. An, J. Shang, and X. Huang. 2019. "Retrieving Surface Soil Moisture over Wheat and Soybean Fields during Growing Season Using Modified Water Cloud Model from Radarsat-2 SAR Data." *Remote Sensing* 11 (16): 1956. doi:[10.3390/rs11161956](https://doi.org/10.3390/rs11161956).
- Yang, H., L. Xie, E. Chen, H. Zhang, G. Yang, Z. Li, and X. Gu. 2016a. "Biomass Estimation of Oilseed Rape Using Simulated Compact Polarimetric SAR Imagery." In *2016 IEEE International Geoscience and Remote Sensing Symposium (IGARSS)*, 5307–5310. Beijing, China: IEEE.
- Yang, Z., K. Li, L. Liu, Y. Shao, B. Brisco, and W. Li. 2014. "Rice Growth Monitoring Using Simulated Compact Polarimetric C Band SAR." *Radio Science* 49 (12): 1300–1315. doi:[10.1002/2014RS005498](https://doi.org/10.1002/2014RS005498).
- Yang, Z., K. Li, Y. Shao, B. Brisco, and L. Liu. 2016b. "Estimation of Paddy Rice Variables with a Modified Water Cloud Model and Improved Polarimetric Decomposition Using Multi-temporal RADARSAT-2 Images." *Remote Sensing* 8 (10): 878. doi:[10.3390/rs8100878](https://doi.org/10.3390/rs8100878).
- Yokota, Y., S. Nakamura, J. Endo, K. Suwa, T. Endo, M. Tsuji, K. Hariu, Y. Kankaku, S. Suzuki, and M. Shimada. 2015. "Evaluation of Compact Polarimetry and along Track Interferometry as Experimental Mode of PALSAR-2." In *2015 IEEE International Geoscience and Remote Sensing Symposium (IGARSS)*, 4125–4128. Milan, Italy: IEEE.
- Zhang, W., Z. Li, E. Chen, Y. Zhang, H. Yang, L. Zhao, and Y. Ji. 2017. "Compact Polarimetric Response of Rape (*Brassica Napus L.*) At C-Band: Analysis and Growth Parameters Inversion." *Remote Sensing* 9 (6): 591. doi:[10.3390/rs9060591](https://doi.org/10.3390/rs9060591).

Appendix Relationship between PAI and wet biomass

We fit the regression models between PAI and wet biomass of rice to find the best relationship among them. The power trend line is best fitted to the 2019 data sets with a correlation of determination (R^2) of 0.75, as shown in [Figure A](#). The associated distribution of PAI and wet biomass values throughout several phenological stages is also highlighted next to the x- and y-axis.

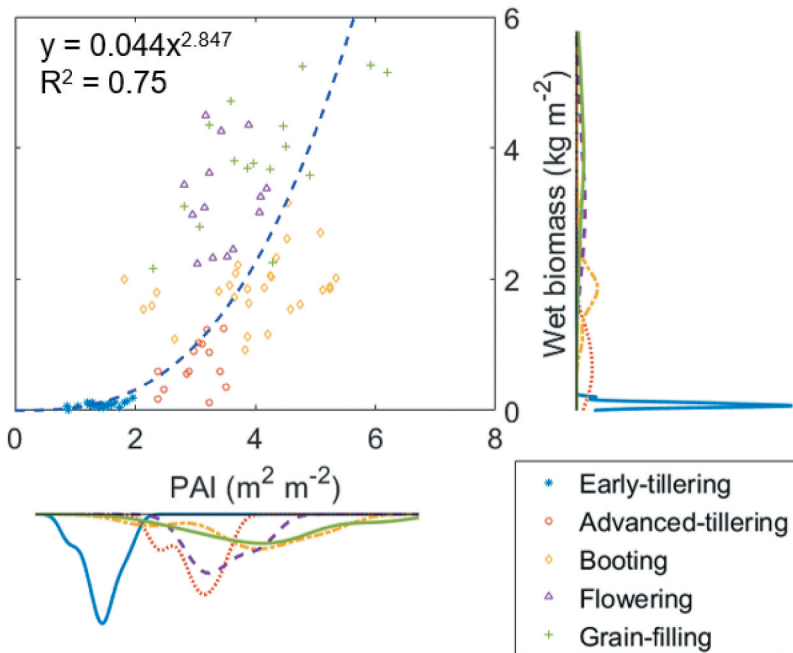


Figure A. Relationship between in-situ measured PAI ($\text{m}^2 \text{ m}^{-2}$) and wet biomass (kg.m^{-2}) of rice for 2019 data sets.